Published in "Inorganic Chemistry 50(16): 7460–7477, 2011"
which should be cited to refer to this work.

Detailed Ab Initio First-Principles Study of the Magnetic Anisotropy in a Family of Trigonal Pyramidal Iron(II) Pyrrolide Complexes

Mihail Atanasov,*[,†,§,∥] Dmitry Ganyushin,[†] Dimitrios A. Pantazis,[†,‡] Kantharuban Sivalingam,[†] and Frank Neese*[,†,‡]

[†]Institute for Physical and Theoretical Chemistry, University of Bonn, Wegelerstrasse 12, D-53115 Bonn, Germany

[‡]Max-Planck Institute for Bioinorganic Chemistry, Stiftstrasse 32-34, D-45470 Mülheim an der Ruhr, Germany

[§]Institute of General and Inorganic Chemistry, Bulgarian Academy of Sciences, Acad. Georgi Bontchev Street 11, 1113 Sofia, Bulgaria

[∥]Département de Chimie, Université de Fribourg, Ch. du Musée, 9, CH-1700 Fribourg, Switzerland

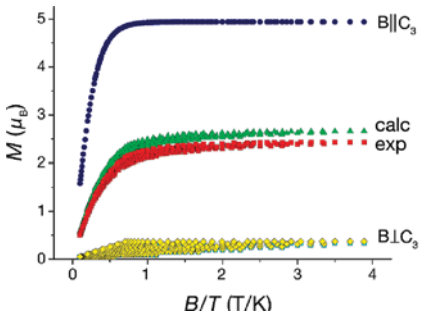

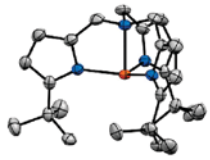

ABSTRACT: A theoretical, computational, and conceptual framework for the interpretation and prediction of the magnetic anisotropy of transition metal complexes with orbitally degenerate or orbitally nearly degenerate ground states is explored. The treatment is based on complete active space self-consistent field (CASSCF) wave functions in conjunction with *N*-electron valence perturbation theory (NEVPT2) and quasidegenerate perturbation theory (QDPT) for treatment of magnetic field- and spin-dependent relativistic effects. The methodology is applied to a series of Fe(II) complexes in ligand fields of almost trigonal pyramidal symmetry as provided by several variants of the tris-pyrrolylmethyl amine ligand (tpa). These systems have recently attracted much attention as mononuclear single-molecule magnet (SMM) complexes. This study aims to establish how the ligand field can be fine tuned in order to maximize the magnetic anisotropy barrier. In trigonal ligand fields high-spin Fe(II) complexes adopt an orbitally degenerate ^5E ground state with strong in-state spin−orbit coupling (SOC). We study the competing effects of SOC and the $^5E\otimes\varepsilon$ multimode Jahn−Teller effect as a function of the peripheral substituents on the tpa ligand. These subtle distortions were found to have a significant effect on the magnetic anisotropy. Using a rigorous treatment of all spin multiplets arising from the triplet and quintet states in the d^6 configuration the parameters of the effective spin-Hamiltonian (SH) approach were predicted from first principles. Being based on a nonperturbative approach we investigate under which conditions the SH approach is valid and what terms need to be retained. It is demonstrated that already tiny geometric distortions observed in the crystal structures of four structurally and magnetically well-documented systems, reported recently, i.e., $[Fe(tpa^R)]^-$ (R = *tert*-butyl, Tbu (**1**), mesityl, Mes (**2**), phenyl, Ph (**3**), and 2,6-difluorophenyl, Dfp (**4**), are enough to lead to five lowest and thermally accessible spin sublevels described sufficiently well by $S = 2$ SH provided that it is extended with one fourth order anisotropy term. Using this most elementary parametrization that is consistent with the actual physics, the reported magnetization data for the target systems were reinterpreted and found to be in good agreement with the ab initio results. The multiplet energies from the ab initio calculations have been fitted with remarkable consistency using a ligand field (angular overlap) model (ab initio ligand field, AILFT). This allows for determination of bonding parameters and quantitatively demonstrates the correlation between increasingly negative *D* values and changes in the σ-bond strength induced by the peripheral ligands. In fact, the sigma-bonding capacity (and hence the Lewis basicity) of the ligand decreases along the series **1** > **2** > **3** > **4**.

I. INTRODUCTION

In this work we study the origin of the magnetic anisotropy of a family of trigonal pyramidal iron(II) complexes supported by derivatives of the tris(pyrrolyl-α-methyl) ligand. It was recently discovered that these systems possess unusually large magnetic anisotropies.[1,2] The computational and theoretical results reported here are used to analyze the effects of the geometrical distortions due to the first coordination sphere (Jahn−Teller effect) and the influence of the remote ligand substituents on the magnetic anisotropy.

Single-molecule magnets (SMMs) are molecules that exhibit slow magnetic relaxation, which originates from an energy barrier to inversion of the total molecular spin. The magnetic moment can eventually be blocked if the thermal energy is smaller than the barrier height. This slow relaxation enables such molecules to act as molecular magnets, similar to the classical ones. This behavior manifests itself by the presence of a magnetic hysteresis at low

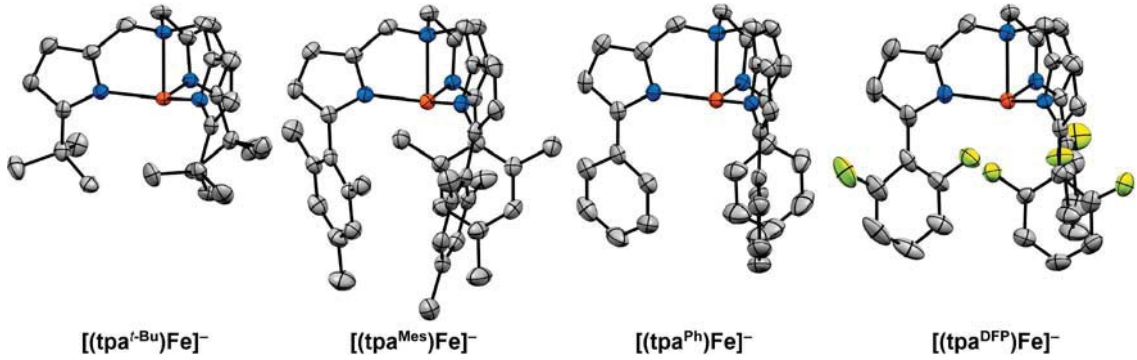

Figure 1. Structures of trigonal pyramidal FeN_4 tpa-based complexes with SMM properties. Orange, blue, yellow, and gray ellipsoids represent Fe, N, F, and C atoms, respectively. Hydrogen atoms have been omitted for the sake of clarity (adopted from ref 2).

temperature. The discovery of SMMs nearly 20 years ago[3] has induced large-scale research efforts since such species might ultimately find applications in high-density information storage,[4] quantum computing,[5−7] or even magnetic refrigeration.[8] However, successful design of SMMs rests on the ability to find molecules with a sufficiently large magnetic anisotropy such that the blocking temperature is raised from nearly zero to more practical values, ideally room temperature. Clearly, this ultimate and ambitious goal requires a clear understanding of the magne-to-structural correlations that dominate the magnetic anisotropy.

Experimental and theoretical studies on manganese-based, oxo-bridged SMMs have been used to explore the parameters that govern the spin-reversal barriers in such complexes.[9] This barrier has been expressed as $U = S^2|D|$, where S is the spin ground state and D is the axial zero-field splitting parameter that quantifies the magnitude of the magnetic anisotropy. In addition to S and D, the magnitude of the magnetic exchange coupling between constituent metal centers in a SMM, J, serves to define the temperature range over which the barrier is effective, since it determines how well isolated in energy the spin ground state is from excited states. Despite the requirement of large S and D, efforts to increase these parameters simultaneously have been prohibited by their interrelationship, where it has been shown already in ref 10 that D is inversely proportional to S^2 and thus $U = S^2|D|$ does not or only weakly depends on the ground state total spin. The importance of this result for single-molecule magnetism has been only recently recognized.[11−13] Note that the proportionality of D to $1/S^2$ is not specific to the case of magnetically interacting ions in clusters but is a fundamental result of rigorous theory as described in detail in ref 10. It has already been verified experimentally that clusters exhibiting large values of S tend to show small values of D.[9] For instance, in the highest spin ground state yet observed for a molecule, $S = 83/2$,[14] D is so small that no slow magnetic relaxation could be detected, despite the comparatively large local anisotropy due to the Mn(III) ions involved in the cluster.

In Mn(III)-based oxo-bridged SMMs the magnetic anisotropy stems from nearly parallel alignments of the Mn(III) local spins arising from Jahn−Teller splitting of its ^5E ground state and the spin−orbit coupling (SOC) of the resulting orbitally nondegenerate ground state with excited electronic states ($^5T_2$) bearing angular momenta. Magnetic anisotropies described by a total D of this origin cannot become large. Thus, recently attention has been turned to transition metal ions with orbitally (nearly) degenerate ground states. Such states with strong in-state SOC

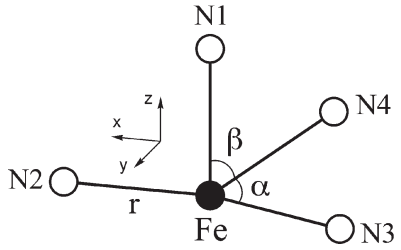

Figure 2. Geometrical parameters, numbering of ligator atoms of FeN_4^- complexes, definition of the geometrical parameters r, α, and β, and orientation of the Cartesian axes with respect to the molecular frame.

arise in certain d^N configurations, provided that a 3- or 4-fold axis is present. In such systems, the energy gap U can become larger than 100 cm^{-1} even in complexes with first-row transition metals.[1,2] Due to much larger SOC the magnetic anisotropies are largely enhanced in rare earth (4f) or actinide (5f) complexes.[15−19] Orbital moments of transition 3d, 4d, and 5d complexes are usually quenched by off-axial geometric distortions;[20−28] however, using geometrically constrained and sterically bulky macrocyclic ligands it was possible to stabilize low-coordinate high-spin iron(II) complexes[29−34] with axial D values as large as −50 cm^{-1} in a planar (β-diketiminate)$FeCH_3$ complex.[29]

Recently, hybrid ligand scaffolds of Fe(II) with trianionic tris-(pyrrolyl-α-methyl)amines[35] have been reported to display a 3-fold coordination geometry around the Fe(II) center and an unusually large value of $D = -40$ cm^{-1} as found in K[Fe(tpa^{Mes})].[1] Slow relaxation of the magnetization in the presence of a small dc field with an effective relaxation barrier of $U_{eff} = 42$ cm^{-1} provides the first example of a mononuclear transition metal complex with a SMM-like behavior.[1]

Expanding on this discovery, a series of four (Figures 1 and 2) structurally and magnetically well-documented compounds, [Fe(tpa^R)]$^-$ (R = *tert*-butyl, Tbu (**1**), mesityl, Mes (**2**), phenyl, Ph (**3**), and 2,6-difluorophenyl, Dfp (**4**) have been reported to display similar properties tuned by a variation of the substituents R.[2] Using the same compounds oxygen-atom transfer properties, intramolecular aromatic C−H hydroxylation (for **3**, $Me_3NO \rightarrow Me_3N + O$), activation of nitrous oxide ($N_2O \rightarrow N_2 + O$), and intermolecular hydrogen-atom abstraction (for **2**) have been demonstrated.[35]

Calculations of the electronic structure and magnetic properties of complexes with orbitally degenerate or nearly degenerate ground states represent a real challenge for first-principles methods. DFT-based perturbation theory is not directly applicable because of the multireference nature of such ground states. Note, however, that a general DFT-based ligand field approach to the parameters of the spin Hamiltonian (SH), LFDFT, has been proposed.[27,36−38] At the same time, the systems under consideration are too large to be treated by the usual implementations of variational configuration interaction (CI) approaches that cover dynamic correlation effects. Even the application of complete active space self-consistent field (CASSCF)[39] in conjunction with second-order perturbation corrections of the CASSCF energies (such as the complete active space perturbation theory, CASPT2,[40−44] or the *N*-electron-valence-perturbation theory, NEVPT2) is very challenging.[45−48] The potential of using such approaches to calculate SH parameters of mononuclear[13,49] and binuclear[50−52] transition metal complexes has been recently demonstrated. A general first-principles method to calculate the spin-dependent part of the energy of ground and excited multiplet energies in larger polynuclear complexes has been proposed.[53] Here, we apply the recent implementation of the CASSCF and NEVPT2 methods in our computer code ORCA[54] to perform large-scale correlated calculations on systems of an unprecedented size. The results presented in this work provide a theoretical, computational, and conceptual framework for interpretation, analysis, and prediction of the magnetic anisotropy in transition metal complexes with orbitally degenerate or nearly degenerate ground states.

Using this first-principles method we study the effects of the small $^5E\otimes\varepsilon$ multimode Jahn−Teller distortions and the influence of the substituents of the tpa ligand on the magnetic anisotropy by a full rigorous treatment of all spin multiplets stemming from the quintet and triplet states within the d^6 configuration of Fe(II) and by an approximate effective SH approach. The comparison between these two independent treatments allows one to specify in which cases and under which conditions the SH approach is still valid. Furthermore, it becomes evident which terms are minimally required in the SH in order to describe the actual level structure correctly. We show below that the tiny geometric distortions observed in the crystal structures of the well-documented systems reported recently ($[Fe(tpa^R)]^-$ **2**, **3**, and **4** (Figure 1) are enough to lead to only five low-lying and thermally accessible spin $S = 2$ sublevels described sufficiently well by a $S = 2$ spin Hamiltonian, provided that it is extended with one fourth-order tensor spin operator. Using this approach, the reported magnetization data have been reinterpreted and found to be in good agreement with the ab initio results. Furthermore, the multiplet energies from the ab initio calculations have been fitted with remarkable consistency using a ligand field (angular overlap) model (ab initio ligand field), thus allowing one to deduce bonding parameters. Using this approach one is able to explore the dependence of D on the geometric and electronic structure of the ligand system.

II. THEORY AND COMPUTATIONS

II.1. Computational Details. Since the results of the calculations are expected to be sensitive to small structural details, we conducted the calculations on the four compounds (**1**−**4**) on the basis of both crystal and optimized structures. Geometry optimizations have been performed using the nontruncated systems along with the Perdew−Becke−Ernzerhof (PBE) functional,[55] empirical van der Waals corrections[56] for the DFT energy, the scalar relativistic zero-order regular approximation (ZORA),[57] and the scalar relativistically recontracted (SARC)[58] version of the def2-TZVP basis set.[59]

Ground and excited state energies and wave functions as well as magnetic properties were calculated on geometries from X-ray diffraction data[1,2] and from DFT geometry optimizations using the CASSCF module of ORCA (to account for static correlation) together with the *N*-electron valence perturbation theory (NEVPT2)[45−48] (to account for dynamic correlation). Unlike the popular CASPT2 method, NEVPT2 does not suffer from intruder state problems because the important two-electron interactions inside the active space are already included in the definition of the zeroth-order Hamiltonian.[60] This results in a spectrum of the zeroth-order Hamiltonian that is much closer to the spectrum of the full Hamiltonian than what one can achieve with a one-body zeroth-order Hamiltonian. This ensures properly positive and sufficiently large energy denominators that are imperative for a stable perturbation series. In CASPT2 one needs to introduce level shift parameters in the energy denominators in order to avoid divergence. The final energies then depend on the user defined level shift.[61,62]

The nontruncated systems **1**−**4** were used in the calculations. It is worth emphasizing that this is essential to obtain realistic results. Truncated versions of the systems only capture a fraction of the differences in magnetic properties observed experimentally. This will be elaborated below.

For the correlated calculations, basis sets of def2-TZVPP, def2-TZVP, def2-SVP, and def2-TZVP(-f) quality for Fe, N, H, and C, respectively, alongside with the corresponding auxiliary sets have been used.[54] In this set of calculations only the metal d orbitals were included in the active space. According to conventional wisdom, this set is too small as a second d shell is usually required in CASPT2 calculations along with the corresponding metal−ligand bonding orbitals. Technically, these extensions do not present essential problems; however, our preliminary calculations with extended active spaces did not improve the results noticeably. Hence, in keeping with Ockham's razor, we used the smallest possible active space that cleanly maps onto ligand field theory. The fact that inclusion of metal−ligand bonding orbitals is not necessary probably stems from the limited covalency between high-spin Fe(II) and the ligand. We do not expect this to be a universal conclusion for CASSCF/NEVPT2 calculations.

Realistic treatment of SOC is crucial for successful modeling of the magnetic properties. In a ^5E orbitally degenerate ground state SOC occurs in the first order of perturbation theory (PT) but generally at second order for orbitally nondegenerate states with $S > 1/2$. This leads to mixing of states which differ in their spin by $\Delta S = \pm 1,0$. Through this mixing, SOC reintroduces some orbital angular momentum into the electronic ground state that is otherwise well known to be quenched through low symmetry. In QDPT,[63] one starts by obtaining an approximate solution of the Born−Oppenheimer (BO) Hamiltonian of a multireference type such as CASSCF in the form given by

$$|\Psi_I^{SS}\rangle = \sum_\mu C_{\mu I}|\Phi_\mu^{SS}\rangle \tag{1}$$

where the upper indices SS stand for a many-particle wave function (configuration state function, CSF) with a spin quantum number S and spin projection quantum number $M_S = S$. SOC lifts the $(2S + 1)$ degeneracy of the total spin S of $\hat{H}_{BO}$ eigenfunctions. Thus, the basis for the SOC treatment are the $|\Psi_I^{SS}\rangle$ states, in which I extends to all states calculated in the first step of the procedure and $M_s = -S...S$ labels all members of a given term. Matrix elements of SOC over the $|\Psi_I^{SM_s}\rangle$ basis functions are easily generated making use of the Wigner−Eckart theorem, since all $(2S + 1)$ term components share the same spatial part of the wave function.[64] In this way, both the SOC and the Zeeman interaction can be accurately accounted for.

The Zeeman interaction can be accounted for by diagonalization of the matrix representation $\hat{H}_{BO} + \hat{H}_{SOC} + \hat{H}_Z$ in the $|\Psi_I^{SM_s}\rangle$ basis

$$\langle \Psi_I^{SM_s} | \hat{H}_{BO} + \hat{H}_{SOC} + \hat{H}_Z | \Psi_J^{S'M_s'} \rangle = \delta_{IJ}\delta_{SS'}\delta_{M_sM_s'}E_I^S + \langle \Psi_I^{SM_s} | \hat{H}_{SOC} + \hat{H}_Z | \Psi_J^{S'M_s'} \rangle \quad (2)$$

The complete manifold of 5 quintet and 45 triplet states was included in the calculations, and SOC was accounted for by the mean field (SOMF) Hamiltonian.[65,66] Evaluation of the matrix elements of the orbital momentum operators between the $|\Psi_I^{SM_s}\rangle$ basis functions is done in terms of one-electron matrix elements within the MO basis. This procedure carries us beyond the perturbative regime and accounts for strong SOC effects to all orders. Test calculations additionally including the 50 singlet states did not change the results. Similar to the procedures followed in the closely related CASSCF/CASPT2 methodology with inclusion of SOC,[44] matrix elements were calculated using the state-averaged CASSCF (SA-CASSCF) wave functions and NEVPT2 corrections are only included in the diagonal of the QDPT matrix.

An approximate counterion/solvent modeling using the conductor-like screening model (COSMO)[67,68] was also attempted. However, possibly due to the limited total charge of −1 of the target systems, the results are almost identical to the ones in which the COSMO model was not included.

In order to study vibronic coupling effects (the present systems represent $^5E\otimes\varepsilon$ Jahn−Teller problems) we used a truncated model obtained by freezing the geometry of each Fe(tpa) complex unit and replacing the bulky substituents at the pyrrolyl fragments with hydrogen atoms (C−H bond distances and H−C−C bond angles were reoptimized with the Fe(tpa) geometry unchanged).

II.2. Magnetic Properties. *II.2.1. Exact Treatment within the Manifold of the ^5E Ground Term.* Under the combined action of SOC and vibronic coupling, the ^5E ground state of trigonal Fe(II) splits into 10 sublevels spaced in a narrow interval of 500 cm^{-1}. This manifold is well separated from all other excited states by an energy gap of more than 5000 cm^{-1}.

The leading term in the Hamiltonian consists of the diagonal energies resulting from SA-CASSCF eigenvalues, corrected for dynamical correlation by NEVPT2. Within the complete triplet and quintet manifold of the d^6 configuration, 160 microstates arise that interact via $\hat{H}_{SOC}$. This operator as well as the set of spin $\hat{S}_i$ and angular momentum operators $\hat{L}_i$ ($i = x, y, z$) are represented by off-diagonal (complex valued) 160 × 160 matrices. Denoting the 10 lowest CI eigenvectors of $\hat{H}_{SOC}$ by the rectangular submatrix $\mathbf{C}$(1:160,1:10), the matrices of $\hat{S}_i$ and $\hat{L}_i$ are transformed into the (10 × 10) $\hat{S}_i'$ and $\hat{L}_i'$ matrices of the ^5E model subspace (eqs 3 and 4)

$$\hat{S}_i' = C^\dagger \hat{S}_i C \quad (3)$$

$$\hat{L}_i' = C^\dagger \hat{L}_i C \quad (4)$$

Denoting the diagonal matrix of the 10 $\hat{H}_{SOC}$ lowest eigenvalues by $\hat{\Lambda}$, we then solve the eigenvalue equation for the operator matrix $\hat{H} = \hat{\Lambda} + \hat{H}_Z$ ($\hat{H}_Z$ = the Zeeman matrix) on a grid of points on a unit sphere defined by the vectors (n_x, n_y, n_z) (eq 5) using the value of the probing magnetic field $B = B_o$ (in T) and for the sake of numerical differentiation (see below) two more incremental values $B = B_o + 0.01$ and $B = B_o + 0.02$.

$$\hat{H} = \hat{\Lambda} + \beta B[n_x(\hat{L}_x' + g_0\hat{S}_x') + n_y(\hat{L}_y' + g_0\hat{S}_y') + n_z(\hat{L}_z' + g_0\hat{S}_z')] \quad (5)$$

The field-dependent adiabatic magnetization of a crystalline powder has been calculated using a numerical integration over all magnetic field directions (eq 6, N_A = the Avogadro number, k_B = the Boltzmann constant, Z = the partition function, i.e., the sum of Boltzmann factors for all states under consideration) defined by the vector (n_x, n_y, n_z) or alternatively by the polar angles φ and θ.

$$M_{av} = N_A k_B T \int_0^{\pi}\int_0^{2\pi} \left[\frac{d}{dB(\varphi,\theta)}\ln(Z(B(\varphi,\theta)))\right]\frac{1}{4\pi}\sin^2\theta\, d\theta\, d\varphi \quad (6)$$

Note that this treatment is by definition more accurate than the direct diagonalization of the SOC and magnetic field together in the basis of the nonrelativistic magnetic sublevels of the ^5E term. This is because the SOC of the ^5E state with all other quintet and triplet ligand field states is accounted for to all orders. The only thing that is missing is the magnetic field-induced mixing of the 10 lowest SOC-corrected relativistic eigenstates with the other states. This must be tiny given that the orbital Zeeman matrix elements are on the order of 1 cm^{-1} while the energy differences to the next low-lying SOC-corrected states are, by construction, higher than 5000 cm^{-1}. Technically, the simultaneous diagonalization of the SOC and magnetic field in the entire ligand field manifold would not be a problem of course. However, the present method has the advantage that the effective Hamiltonian obtained in the SOC-corrected 10 × 10 spaces maps most cleanly onto the spin Hamiltonian to be discussed in the next section.

II.2.2. Connection to the Spin Hamiltonian. The ^5E ground state of Fe(II) in trigonal ligand field is described by a spin S =2 and two singly occupied orbitals $e(d_{xz})$ or $e(d_{yz})$ which carry an extra electron in addition to the half-filled $[(d_{xz}d_{yz})^2 d_{z2}{}^1(d_{x2-y2}d_{xy})^2]$ shell. These states give rise to $M_l = \pm 1$ eigenfunctions of the angular momentum operator $\hat{L}_z$(eq 7).

$$|^5E, \pm 1\rangle = (1/\sqrt{2})(|^5E, d_{xz}\rangle \pm i|^5E, d_{yz}\rangle) \quad (7)$$

Since the states $|^5E,1\rangle$ and $|^5E,-1\rangle$ cannot mix by $\hat{L}_x$ and $\hat{L}_y$ (M_l changes by 1 under the action of these operators) and the excited $|^5A_1,0\rangle$ state is much higher in energy[69] (see section III.1, Figure 5), the ^5E ground state SOC operator $\hat{H}_{SOC}$ in this approximation takes the simple form

$$\hat{H}_{SOC} = -(\zeta/4)\hat{L}_z\hat{S}_z \quad (8)$$

Thus, within the $|M_s,M_l\rangle$ basis $\hat{H}_{SOC}$ is represented by a diagonal 10 × 10 matrix with elements: $-(\zeta/4)M_sM_l$ (M_s = 0, ±1, ±2 and M_l = ±1).[70−74] ζ is the effective (covalently reduced) SOC 'constant' of Fe(II) (see ref 75 for a detailed discussion). On symmetry lowering from C_{3v} to C_s or even C_1, the $^5E(d_{xz})$ and $^5E(d_{yz})$ sublevels split and mix with each other, as described by the two energy parameters δ_1 and δ_2, respectively (eq 9). Thus, within the basis of eq 7 the ligand field operator $\hat{H}_{LF}$ (eq 10) is off-diagonal; It mixes the terms $|M_s,1\rangle$ and $|M_s,-1\rangle$.

$$\begin{array}{c} {}^5E(d_{xz}){}^5E(d_{yz}) \\ \begin{bmatrix} -\delta_1 & \delta_2 \\ \delta_2 & \delta_1 \end{bmatrix} \end{array} \quad (9)$$

$$\hat{H}_{LF} = \delta\left(\hat{L}_x^2 - \hat{L}_y^2\right); \delta = -\delta_1 + i\delta_2 \quad (10)$$

The physical origin of δ will be thoroughly analyzed in section II.3. Analytical expressions for the eigenvalues of the matrix $\hat{H}_{SOC} + \hat{H}_{LF}$ (^5E) are given in eq 11 (see Supporting Information for a derivation) along with symmetry notations pertaining to the D_3 holohedrized symmetry. It is worth noting that within the many-electron basis of the ^5E ground term, the A_1 and A_2 states (eq 11) remain accidentally degenerate in the

Table 1. ^{5}E Ground State Multiplet Energies and Spin-Hamiltonian Parameters in Trigonal FeN_4 Complexes in Dependence of Spin−Orbit Coupling (ζ) and off-Axial Splitting (δ)[a]

$\delta = 0$		$\zeta \gg \delta \gg \beta B/2$		$\delta \gg \zeta$	
E	M_J	E	M_S	E	M_S
A_1,A_2: $\zeta/2$	$\pm3/2$	$\zeta/2$	±2	$\delta + \zeta^2/(8\delta)$	±2
E: $\zeta/4$	$\pm1/2$	$\zeta/4$	±1	$\delta + \zeta^2/(32\delta)$	±1
E: 0	$\pm1/2$	$\delta, -\delta$	0,0	$\delta, -\delta$	0,0
E: $-\zeta/4$	$\pm3/2$	$-\zeta/4$	±1	$-\delta - \zeta^2/(32\delta)$	±1
A_1,A_2: $-\zeta/2$	$\pm5/2$	$-\zeta/2$	±2	$-\delta - \zeta^2/(8\delta)$	±2
D: $\zeta/8$		D: $(3\zeta/28) - (\delta/7)$		D: $(\zeta^2/32\delta)$	
B_{40}: 0		B_{40}: $-(\zeta/840) + (\delta/140)$		B_{40}: 0	
g_z: 2		g_z: 1.5		g_z: 2	
$g_{x,y}$: 0		$g_{x,y}$: 0		$g_{x,y}$: 2	
D: $-9\zeta/112$		D: $-(3\zeta/28) + \delta/7$		D: $-(\zeta^2/32\delta)$	
B_{40}: $\zeta/3360$		B_{40}: $(\zeta/840) - (\delta/140)$		B_{40}: 0	
g_z: 2		g_z: 2.5		g_z: 2	
$g_{x,y}$: 0		$g_{x,y}$: 0		$g_{x,y}$: 2	

[a]Entries in the second and third rows include SH paramaters for the lower and upper $S = 2$ nonrelativistic spin multiplets of the ^5E state.

absence of SOC mixing with excited states (see below).

$$E(A_1,A_2) = \pm\frac{1}{2}\sqrt{4\delta^2 + \zeta^2}$$
$$E(E) = \pm\frac{1}{4}\sqrt{16\delta^2 + \zeta^2} \qquad (11)$$
$$E(E) = \pm\delta$$

From eqs 7−10 the origin of the magnetic anisotropy immediately emerges; without off-axial distortions ($\delta = 0$) there is a 1:1 mixing between the xz and yz sublevels of the ^5E term by SOC, and this leads to addition of an orbital angular momentum contribution of 1/2 ($L = 1 = (1/2)g_o$, $g_o = 2$, the electron free spin g factor) to the spin-only value of $S = 2$ in the ground state and subtracts the same amount from the excited state, leading to total spin moments J of these two states of 5/2 (a 'sextet' ground state) and 3/2 (a 'quartet' excited state), respectively. However, these states are split further by SOC even in zero field. It follows immediately (within the approximations inherent in eq 11) that a SH of the usual form for $J = 5/2$ and 3/2 applies to this case. Since $\hat{L}_x = \hat{L}_y = 0$, this SH is of the Ising type. Energies and their corresponding $\hat{J}_z = \hat{S}_z + (1/2)\hat{L}_z$ eigenvalues (M_J, Table 1) along with the spin Hamiltonian of eq 12 ($E = 0$ in this case) have been applied to obtain the ZFS and g-tensor parameters included in Table 1; the value of D is correspondingly negative for $J = 5/2$ (the ground state, Table 1, second row, first column) and positive for the $J = 3/2$ (the excited state, Table 1, third row, first column), and one additional fourth-order term (B_{40}) in the parametrization emerges.

$$\hat{H}^{\text{eff}}_{\text{ZFS}} = D\left[\hat{J}_z^2 - J(J+1)/3\right] + (E/2)\left(\hat{J}_+^2 + \hat{J}_-^2\right) + B_{40}\left[35\hat{J}_z^4 - (30J(J+1) - 25)\hat{J}_z^2 + 3J(J+1)(J(J+1) - 2)\right] \qquad (12)$$

Turning now to the other extreme, $\delta \gg \zeta$, and applying perturbation theory, energy expressions for the zero-field split levels of the two $S = 2$ states can be derived. The resulting expressions for D are listed in Table 1 (third column); a SH of the broadly used form of eq 11 with a negative (positive) D for the ground (excited) state applies in this case

$$\hat{H}^{\text{eff}}_{\text{ZFS}} = D[\hat{S}_z^2 - S(S+1)/3] + E\left(\hat{S}_x^2 - \hat{S}_y^2\right) \qquad (13)$$

In the Fe(II) complexes considered that possess close to trigonal geometries, $\zeta \gg \delta$, i.e., much closer to the case with $\delta = 0$ (eq 12). It is interesting to observe that the lowest A_1 and A_2 states are nondegenerate and thus (being 1:1 mixtures of functions with $M_l = \pm1$, see Supporting Information) nonmagnetic, i.e., $M_J = 0$ in the absence of a magnetic field. However, they become polarized (mixed) by an applied magnetic field which recovers values of $M_J = \pm5/2$ (see Table 1, first column). This causes a Zeeman splitting of $5\beta B$. Off-axial distortions lead to a first-order $\pm\delta$ splitting of the second E ($M_J = \pm1/2$) term which tends to recover pure $^5E(d_{xz})$ and $^5E(d_{yz})$ many-electron wave functions starting from $|M_s, \pm1\rangle$ (eq 7). Thus, it competes with the Zeeman splitting. If $\delta \gg \beta B/2$, the Zeeman splitting is suppressed, thus leading to a dominant $M_J = M_s = 0$ situation which *remains* even with an applied magnetic field. In this particular case one can redefine the SH of eq 12 in terms of a formal spin of $S = 2$ for two noninteracting electronic states with D negative (positive) in the ground (excited) state and correspondingly modified g-tensor values of $g_z = 2.5(1.5)$ ($g_x = g_y = 0$). Under these conditions the SH of eq 13 is still applicable, when extended with a fourth-order tensor operator term represented by the parameter B_{40}, eq 14. This is similar to eq 12 (for energy expressions for D and B_{40} see Table 1, second column). Both the signs and the magnitudes of D and B_{40} are dominated by SOC (ζ) but are reduced by the distortions (δ, Table 1, second column).

$$\hat{H}^{\text{eff}}_{\text{ZFS}} = D\left[\hat{S}_z^2 - S(S+1)/3\right] + (E/2)\left(\hat{S}_+^2 + \hat{S}_-^2\right) + B_{40}\left[35\hat{S}_z^4 - (30S(S+1) - 25)\hat{S}_z^2 + 3S(S+1)(S(S+1) - 2)\right] \qquad (14)$$

We should note that eq 11 is not exact but contains *approximations*, i.e., the neglect of mixing via SOC of ^5E with the excited $^5A_1$ and ^5E and the triplet states. Upon accounting for such a mixing the topmost pair of states A_1 and A_2, which are accidentally degenerate in eq 11, split and shift downward in energy (Figure 3). Comparison with

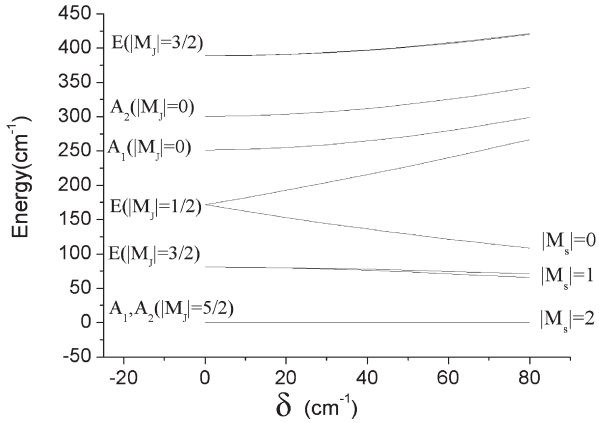

Figure 3. ^5E split sublevels originating from the interplay between the splitting of ^5E (2δ) and the effective spin−orbit coupling parameter ζ deduced from NEVPT2 calculation on $[Fe(tpa^{tbu})]^-$ including the full set of $S = 2$ (5 states) and $S = 1$(45 states). The plot has been constructed using the AOMX program package,[85] along with ligand field parameters obtained from a fit to CASSCF results for (**1**, Table 6b) allowing for a variation of δ.

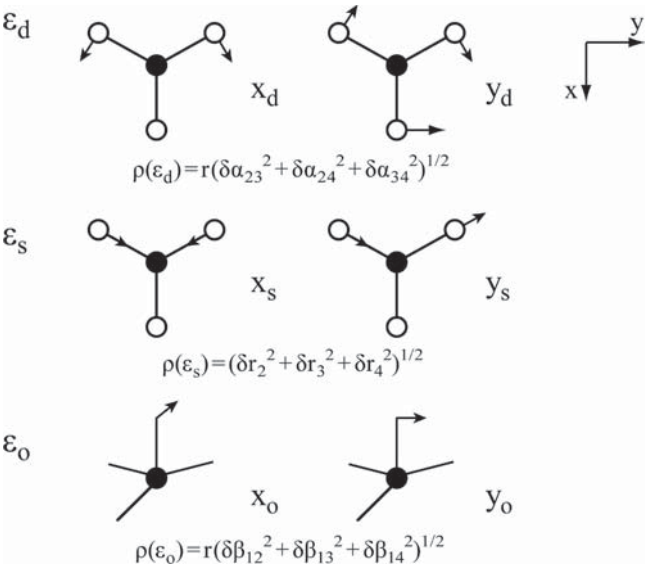

Figure 4. Symmetrized displacements contributing to the Jahn−Teller splitting of the ^5E ground state of the FeN_4 complexes.

exact calculations (see section II.2.1 and results below) shows that the lowest five thermally accessible spin sublevels are well described by the spin Hamiltonian of eq 14 in a quite wide range of δ values; already small distortions described by δ lead to a splitting pattern typical for a $S = 2$ spin with a negative D as illustrated in Figure 3.

Within the basis of the five spin eigenfunctions with $M_s = \pm 2, \pm 1, 0$, the Hamiltonian of eq 14 takes the following matrix form

$$\mathbf{H}_{ZFS} \begin{array}{c} \begin{array}{ccccc} |-2\rangle & |-1\rangle & |0\rangle & |1\rangle & |2\rangle \end{array} \\ \begin{bmatrix} 2D + 12B_{40} & 0 & \sqrt{6}E & 0 & 0 \\ 0 & -D - 48B_{40} & 0 & 3E & 0 \\ \sqrt{6}E & 0 & -2D + 72B_{40} & 0 & \sqrt{6}E \\ 0 & 3E & 0 & -D - 48B_{40} & 0 \\ 0 & 0 & \sqrt{6}E & 0 & 2D + 12B_{40} \end{bmatrix} \end{array} \tag{15}$$

From the separations between the energies of the computed $E(\pm 2 \rightarrow \pm 1)$ and $E(\pm 2 \rightarrow 0)$ levels (cf. diagonal energies of eq 15) D and B_{40} are given by

$$\begin{aligned} D &= -\frac{1}{7}[E(\pm 2 \rightarrow \pm 1) + E(\pm 2 \rightarrow 0)] \\ B_{40} &= \frac{1}{140}\left[E(\pm 2 \rightarrow 0) - \frac{4}{3}E(\pm 2 \rightarrow \pm 1)\right] \end{aligned} \tag{16}$$

and $|E|$ is just 1/6 the off-axial splitting of ± 1.

The parameters of the SH (eq 14) $-D$, B_{40}, E, and additionally g have been fitted to the reported field-dependent magnetization data of complexes **1**−**4** using a nonlinear optimization tool provided by MatLab that minimizes the maximum deviation between the calculated and the experimental values of the magnetization (see Supporting Information for details regarding the fitting). The resulting values of D, B_{40}, and E can then be compared with the ab-initio-computed ones.

II.3. Multimode $^5E\otimes\varepsilon$ Jahn−Teller Effect. The ^5E ground state of trigonal Fe(II) is vibronically unstable and subject to distortions along ε vibrations which can lower the energy and lift the orbital degeneracy. Restricting our attention to linear $^5E\otimes\varepsilon$ Jahn−Teller coupling, the ground state adiabatic potential energy is represented by the matrix of eq 17,[76−78] where K_ε and F_ε are the force constant and linear vibronic coupling parameters, respectively.

$$\begin{bmatrix} (1/2)K_\varepsilon(Q_x^2 + Q_y^2) + F_\varepsilon Q_x & -F_\varepsilon Q_y \\ -F_\varepsilon Q_y & (1/2)K_\varepsilon(Q_x^2 + Q_y^2) - F_\varepsilon Q_x \end{bmatrix} \tag{17}$$

In the complexes under consideration, focusing on the N-donor atoms involved in bonding to Fe(II), there are three types of symmetrized localized modes of ε symmetry involved: two-bending (in- and out-of-plane, ε_d and ε_o) and one stretching (ε_s) whose high- (x or Q_x, $C_{3v} \rightarrow C_s$) and low- (y or Q_y, $C_{3v} \rightarrow C_1$) symmetry components are visualized in Figure 4. In the $[Fe(tpa^R)]^-$ complex these modes are mixed with vibrational coordinates with contributions from all atoms of the tpa macrocycle to give rise to numerous normal modes of the same symmetry.

Thus, the simple eq 17, valid for a single active ε vibration (ideal vibronic system), has to be extended with a number of similar symmetry-related linear vibronic and restoring force terms resulting in a multimode Jahn−Teller problem of the $^5E\otimes(\varepsilon(1) + \varepsilon(2) + ...)$ type. To this end, we apply the formalism for treating such problems described in ref 78. More specifically, it was shown that the adiabatic potential surface of eq 17 extended with all contributing terms can be represented in configurational space in terms of a displacement along a single interaction mode $\varepsilon(q_x,q_y)$ (eq 18).

$$\begin{array}{c} \begin{array}{cc} |^5E, d_{xz}\rangle & |^5E, d_{yz}\rangle \end{array} \\ \begin{bmatrix} (1/2)(q_x^2 + q_y^2) + Fq_x & -Fq_y \\ -Fq_y & (1/2)(q_x^2 + q_y^2) + Fq_x \end{bmatrix} \end{array} \tag{18}$$

In the above expression q_ε, q_ζ, F, and the Jahn−Teller stabilization energy E_{JT} are given in eqs 19−21. The linear vibronic coupling $F_{\varepsilon i}$ and the force constant $K_{\varepsilon i}$ parameters are characteristic of each of the normal modes involved.

$$q_\gamma = \frac{1}{F}\sum_{i=1}^{N_\varepsilon} F_{\varepsilon i} Q_{\gamma i}; \gamma = x, y \tag{19}$$

$$F = \left(\sum_{i=1}^{N_\varepsilon} \frac{F_{\varepsilon i}^2}{K_{\varepsilon i}}\right)^{1/2} \tag{20}$$

$$E_{JT} = \frac{1}{2}\sum_{i=1}^{N_\varepsilon} \frac{F_{\varepsilon i}^2}{K_{\varepsilon i}} \tag{21}$$

The force constant parameters $K_{\varepsilon i}$ are directly accessible from the Hessian matrix, resulting from an ab initio or DFT calculation, while $F_{\varepsilon i}$ can be calculated as follows. Focusing on a given normal mode, described by the set of mass-weighted displacement vectors $q_{\gamma i}(\gamma = x,y)$, we note that because of the localized nature of the $3d^6$ ground state of the Fe(II) complex only movements of the first coordination sphere, i.e., the local modes (Figure 4), contribute to$F_{\varepsilon i}$. This leads to the expression of $F_{\varepsilon i}$ in terms of the local vibronic coupling constants F_ε of eq 22, weighted with the van Vleck coefficients $a_{i\varepsilon}$,[79] i.e., the projection of a given normal mode $q_{\gamma i}(\gamma = x,y)$ on the local mode Q_γ (eq 23). Focusing on the in-plane bending modes ε_d (Figure 4, see Figure 2 for ligand numbering and coordinate orientation) with dominant contributions to the Jahn−Teller activity, $a_{i\varepsilon}$ have been obtained from the scalar product between the vectors $1/(6)^{1/2}(2,-1,-1)$ and $1/(2)^{1/2}(0,1,-1)$ representing the local modes of eqs 24 and 25 and the ab-initio-computed normal modes.

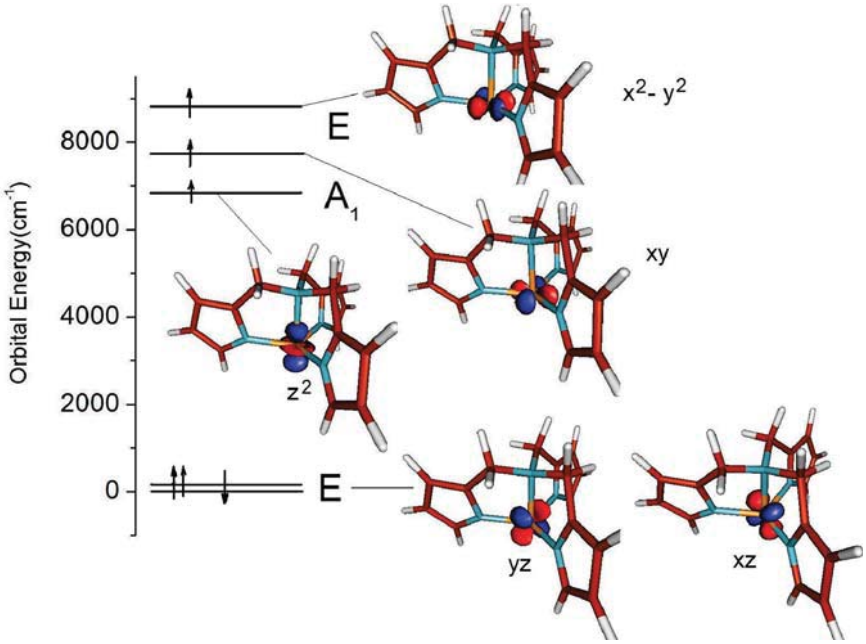

Figure 5. SA-CASSCF orbital shapes and energies and the ground state configuration of $[Fe(tpa)^{Mes}]^-$.

$$F_{\varepsilon i} = \left\langle {}^5E, d_{xz} \middle| \frac{\partial V}{\partial q_{xi}} \middle| {}^5E, d_{xz} \right\rangle = \left\langle {}^5E, d_{xz} \middle| \frac{\partial V}{\partial Q_x} \middle| {}^5E, d_{xz} \right\rangle \frac{\partial Q_x}{\partial q_{xi}} = a_{i\varepsilon} F_\varepsilon \tag{22}$$

$$Q_\gamma = \sum_{i=1}^{N_\varepsilon} a_{i\varepsilon} q_{\gamma i}; (\gamma = x, y) \tag{23}$$

$$Q_x = \frac{1}{\sqrt{6}} R(2\delta\alpha_{34} - \delta\alpha_{23} - \delta\alpha_{24}) \tag{24}$$

$$Q_y = \frac{1}{\sqrt{2}} R(\delta\alpha_{23} - \delta\alpha_{24}) \tag{25}$$

$$F_\varepsilon = \sqrt{E_{FC}/(2\sum_{i}^{N_\varepsilon} a_{i\varepsilon}^2/K_\varepsilon)} \tag{26}$$

Within the approximation of a linear ${}^5E\otimes\varepsilon$ Jahn−Teller coupling (eq 18), the Jahn−Teller stabilization energy E_{JT} (eq 21) is just 1/4 of the ${}^5E$ energy splitting E_{FC}, the energy of the Franck−Condon (FC) transition from the lower to the upper sheet of adiabatic potential energy surface taken at the ground state equilibrium geometry. Adopting a value of E_{FC} as given by the CASSCF(NEVPT2) results, the value of the unknown parameter F_ε has been fixed using eq 26, as derived from combination of eqs 21 and 22.

II.4. Ligand Field Interpretations of the ab Initio Data. Significant insight in terms of familiar chemical concepts can be obtained by mapping the ab initio results onto ligand field theory. This might be viewed as another effective Hamiltonian treatment. While above we restricted our attention to the magnetic sublevels arising from the ${}^5E$ manifold, we here focus on the entire subset of ligand field excited states and their parametric representation in terms of the angular overlap model (AOM)[80−83] variant of ligand field theory.[84] This results in bonding parameters that are to a large extent transferable between systems. Here, multiplet energies are expressed in terms of one-electron matrix elements between molecular orbitals (MOs) with dominant d character, thus defining an effective (5 × 5) ligand field matrix that describes the anisotropic interaction of the central metal orbitals with the ligand orbitals. Interelectronic repulsion and SOC are accounted for, as usual, by covalently reduced atom-like parameters B, C (Racah parameters), and ζ.

The AOM introduces perturbations on the metal d electrons from well-aligned ligand σ and π orbitals, which are described by energy increment parameters e_σ and e_π, respectively. These parameters are specific to the chemical nature of the ligand and also depend on the metal−ligand distance. In addition, factors that solely reflect the angular distribution of the ligands around the metal (e.g., the symmetry of the ligand field) are introduced. They are calculated from the actual structure of the system, without any fitting or arbitrariness. For complexes **1**−**4** with geometries close to trigonal and a planar FeN_3 moiety, the (5 × 5) AOM matrix takes a block diagonal form given by eqs 27 and 28 for the (d_{yz}, d_{x2-y2};d_{xz}, d_{xy}) and d_{z2} orbital sets of e and a_1 symmetry, respectively. The parameters e_σ^e and e_σ^a describe σ-antibonding interactions with the equatorial pyrrolide and axial amine ligands, while $e_{\pi s}^e$ reflects the effect due to the out-of-plane orbitals of the pyrrolide ligand. With $\psi = 0°$ (in this case the pyrrolide ring makes a dihedral angle γ of 90° with the FeN_3 plane, $\psi = 90 - \gamma$) the antibonding effect of $e_{\pi s}^e$ on the $d_{yz}(d_{xz})$ orbitals is minimal, whereas on the $d_{x2-y2}(d_{xy})$ orbitals it is maximal.

$$\begin{array}{cc} e\ d_{yz}(d_{xz}) & d_{x2-y2}(d_{xy}) \end{array}$$
$$\begin{bmatrix} (3/2)(\sin^2\psi)e_{\pi s}^e & (3/4)\sin(2\psi)e_{\pi s}^e \\ (3/4)\sin(2\psi)e_{\pi s}^e & (3/8)[4(\cos^2\psi)e_{\pi s}^e + 3e_\sigma^e \end{bmatrix} \tag{27}$$

$$a_1 d_{z2} : (3/4)e_\sigma^e + e_\sigma^a \tag{28}$$

The set of ligand field parameters e_σ, e_π, B, C, and ζ are usually adjusted with respect to high-resolution spectroscopy.[81−83] However, quite frequently, this is a seriously underdetermined problem; usually there are more parameters than observables. Here we follow the opposite route and take the ab initio results as a much more comprehensive numerical database for the AOM parametrization.

The AOM model is applied in a stepwise procedure as follows: We start with the energies of the four spin-allowed ligand field excitations following their assignment. These transition energies are not directly

Table 2. Fe−N Bond Distances (in Å) and N−Fe−N Bond Angles (in °) of the FeN_4 Chromophore from X-ray Diffraction Data and DFT Geometry Optimization[a]

	$[Fetpa^{Tbu}]^-$		$[Fetpa^{Mes}]^-$		$[Fetpa^{Ph}]^-$		$[Fetpa^{Dfp}]^-$	
	exp. geometry	DFT geometry	exp. geometry	DFT geometry	exp. geometry	DFT geometry	exp. geometry	DFT geometry
r_1	2.144	2.187	2.172	2.218	2.161	2.229	2.196	2.229
r_2	2.031	1.989	2.008	1.992	2.013	1.989	2.042	2.005
r_3	2.031	1.995	2.041	2.014	2.019	1.993	2.038	2.009
r_4	2.031	1.996	2.024	2.015	2.016	1.995	2.037	2.013
α_{23}	118.35	117.93	117.35	116.02	120.22	118.64	115.82	116.99
α_{24}	118.35	118.72	115.28	118.77	115.56	119.31	121.57	119.88
α_{34}	118.35	117.33	122.38	119.48	120.27	116.53	116.63	116.35
β_{12}	82.55	81.86	82.45	82.46	83.84	82.27	81.19	81.27
β_{13}	82.55	81.83	82.01	81.89	83.37	82.36	82.30	80.73
β_{14}	82.55	81.68	83.21	81.62	82.88	81.80	82.01	81.78

[a] See Figure 2 for ligand numbering and definitions.

affected by the parameters B and C. We adjust the parameters e^e_σ, e^a_σ, and $e^e_{\pi s}$ of the Fe−N bonds from a best fit to these transitions. In the second step, we adopt these one-electron parameters without changes and obtain the parameters B and C from the computed energies of the spin-forbidden transitions. In the present case these are the transitions from the ^5E ground state to the triplet ligand field excited states. Finally, adopting the values of e_σ, e_π, B, and C and switching on the SOC, we fix the value of ζ from the computed energies of the ^5E ground state SOC split sublevels. These calculations have been done by interfacing the ORCA program with the well-established ligand field program AOMX.[85] The use of artificially high symmetry was allowed for the sake of simplifying the assignments.

III. RESULTS AND DISCUSSION

III.1. Chemical Bonding, Geometric Structures, and Vibronic Activity. The ground state structures and properties of the $[Fe(tpa^R)]^-$ series are governed by the Fe−tpa bonding interactions, which are reflected in the shapes and energies of the MOs dominated by 3d functions of Fe(II). This is illustrated in Figure 5, taking $[Fe(tpa^{Mes})]^-$ as an example. With the purely π-type $d_{xz,yz}$ and the σ-antibonding d_{z2} and d_{xy},d_{x2-y2} orbitals (eqs 27 and 28), an orbital energy ordering typical for a trigonal pyramidal complex results. The absence of a second axial ligand, due to steric hindrance of the bulky tpa^R ligands, leads to considerable stabilization (included in eq 28 in the parameter e^a_σ) of the d_{z2} orbital due to $3d_{z2}$−4s mixing with respect to the d_{xy},d_{x2-y2} orbitals. However, this stabilizing effect is not strong enough to place d_{z2} below the d_{xz},d_{yz} pair of orbitals. Thus, a ground state of ^5E symmetry with an extra electron of π-type results. The underlying Fe−tpa interaction will be quantified following a ligand field analysis of the ab initio results in section III.4.

The coordination geometry around Fe(II) in all four compounds is close to trigonal with one longer bond to the axial N-ligand from the amino group (mean value over reported X-ray structures of 2.17 Å) and three shorter bonds to the pyrrolyl N donors in the equatorial plane (2.03 Å). The Fe ion is displaced significantly (by 0.26 Å) from the plane defined by the three pyrrolyl N ligands. Bond distances and bond angles relevant for the following discussion are defined in Figure 2, and their values from X-ray data are listed in Table 2; these are the Fe−N bond distances (r_i), N−Fe−N bond angles α_{ij} between the equatorial Fe−N bonds, and the β_{ij} angles formed between the axial and the equatorial Fe−N bonds.

DFT geometry optimizations of the entire complexes yield geometric parameters in good agreement with values reported from X-ray data (Table 2).[35,2] Calculations of the Hessian and the complete vibrational spectrum show that optimized structures for complexes **3** and **4** correspond to minima of the ground state potential energy surface. For complex **2** two imaginary frequencies are obtained. The latter are found to be due to skeletal vibrations with main participation from the pyrrolyl fragments. No vibrational spectrum could be calculated for complex **1**, for which the optimized geometry is found to be closest to trigonal. The reason is that for nearly orbitally degenerate systems the numerical second-derivative treatment becomes unstable as tiny distortions change the electronic ground state and hence drastically change the directions of the obtained forces.

For convenience, the geometric parameters can be represented in terms of their deviations from axial symmetry. Such deviations are clearly discernible, both in the experimental structures and, to a lesser extent, in the optimized structures as well (Table 2). For **1** a regular trigonal structure has been reported,[2] whereas the DFT-optimized structure is significantly distorted. The presence of such a distortion is consistent with the magnetic behavior of **1** as will be discussed in section III.3.

The low-symmetry distortions of the first coordination sphere of Fe(II) are rather complex and can originate from the Jahn−Teller activity of the ^5E ground state as well as from steric effects imposed by the rigid ligand backbone and from the counterions in the solid. In order to shed more light on these issues, a hypothetical complex was calculated that involved the non-Jahn−Teller active Mn(II) ion instead of Fe(II). The corresponding optimized structure was found to be nearly perfectly axial (Table S1 in the Supporting Information). Thus, we conclude that the off-axial distortions are largely due to Jahn−Teller activity. These distortions can be quantified using the Jahn−Teller radii ρ corresponding to the local modes of ε symmetry, two bending and one stretching mode (defined in Figure 4 and listed in Table 3a).

They show that displacements along the FeN_3 bending mode ε_d are dominant. Further analysis of these distortions shows, in agreement with the epikernel principle,[86,87] that the

Table 3. Geometrical Distortions (in Å) of the $Fe^{II}N_4$ Cores in tpa Complexes As Quantified by the Jahn–Teller Radii ρ Deduced from Experimental X-ray Data and DFT Geometry Optimization (a); Decomposition of the Distortions of FeN_4 As Given by X-Ray Diffraction Structures along the High-Symmetry (Q_x, C_s) and Low-Symmetry (Q_y, C_1) Components of the in-Plane Bending Mode ε_d (Figure 4) (b); Contributions of the ε Normal Modes to the Vibronic Coupling Constants $F_{\varepsilon i}$ and the Jahn–Teller Stabilization Energies E_{JT}(i) in the Multimode $^5E\otimes(\varepsilon(1) + \varepsilon(2)...)$ Jahn–Teller Effect in $[FeN_4C_{15}H_{15}]^-$ and $[FeN_3H_6]^-$ Truncated Model Complexes (c)

	$[Fetpa^{Tbu}]^-$		$[Fetpa^{Mes}]^-$		$[Fetpa^{Ph}]^-$		$[Fetpa^{Dfp}]^-$	
(a)	X-ray	DFT	X-ray	DFT	X-ray	DFT	X-ray	DFT
$\rho(\varepsilon_s)$	0	0.005	0.023	0.018	0.004	0.004	0.004	0.006
$\rho(\varepsilon_d)$	0	0.034	0.182	0.090	0.134	0.071	0.158	0.093
$\rho(\varepsilon_o)$	0	0.005	0.031	0.022	0.024	0.015	0.029	0.027

(b)	$[Fetpa^{Mes}]^-$	$[Fetpa^{Ph}]^-$	$[Fetpa^{Dfp}]^-$
Q_x	0.175	−0.134	0.157
Q_y	0.052	0.001	0.018

(c) $\hbar\omega_i$ (cm^{-1})	$F_{\varepsilon i}$ (cm^{-1}/Å)[c]	E_{JT}(i) (cm^{-1})
$[FeN_4C_{15}H_{15}]^-$		
38[a]	−87.5	11.4
121[a]	−278.0	11.3
193[a]	−168.4	1.6
226[a]	156.7	1.0
		$E_{JT(total)}$ 28.4
$[FeN_3H_6]^-$		
57[b]	−229.6	73.6
86[b]	202.9	25.3
97[b]	−124.7	7.4
530[b]	−390.4	2.4
		$E_{JT(total)}$ 111.3

[a] On the basis of a force field of a geometry-optimized, nondistorted $[MnN_4C_{15}H_{15}]^-$ model complex. [b] On the basis of a force field of a geometry-optimized, nondistorted $[MnN_3H_6]^-$ model complex. [c] Calculated adopting values of F_ε (eq 22) of 1133 cm^{-1}/Å and 2653 cm^{-1}/Å and the NEVPT2 ^5E splittings of $[FeN_4C_{15}H_{15}]^-$ and $[FeN_3H_6]^-$ model complexes, respectively.

high-symmetry (C_s) distortion $Q_x(x)$ prevails over the low-symmetry (C_1) one $Q_y(y)$ (Table 3b) and thus determines to a large extent the magnitude of the total $\rho = (Q_x^2 + Q_y^2)^{1/2}$. Following the formalism of section II.3 we analyzed the multimode $^5E\otimes(\varepsilon(1) + \varepsilon(2)...)$ Jahn–Teller effect using truncated model complexes $[FeN_4C_{15}H_{15}]^-$ (I, Figure 6a) and $[MnN_4C_{15}H_{15}]^-$ (II). The first one was used in order to obtain the parameters $F_{\varepsilon i}$, while the second one was used to obtain a reliable Hessian, avoiding the complications from additional quadratic vibronic coupling terms present in I.[88] In these complexes we replaced the bulky substituents of the pyrrolyl fragments by hydrogen atoms (Figure 6a). From the normal modes with ε symmetry only four contribute to a very small total Jahn–Teller stabilization energy

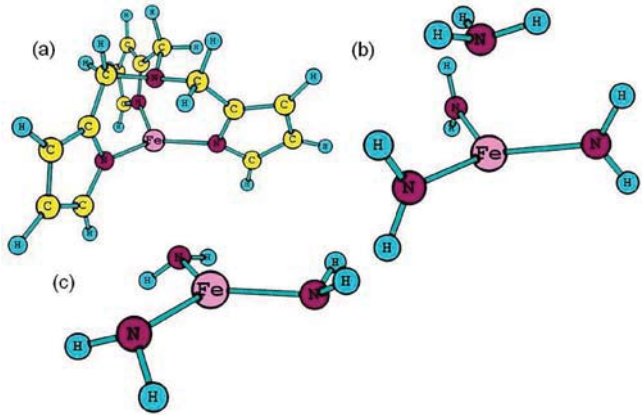

Figure 6. Truncated model clusters adopted for the study of the vibronic effects within the ^5E ground state manifold: (a) Truncated model complex $[FeN_4C_{15}H_{15}]^{1-}$ employed in the study of the $E\otimes\varepsilon$ Jahn–Teller effect; (b) $[FeN_4H_9]^-$ model complex with three unlinked equatorial NH_2^- amido groups; (c) $[FeN_3H_6]^-$ model fragment resulting upon dissociation of $[FeN_4H_9]^-$.

$E_{JT(total)}$ = 28.4 cm^{-1} (Table 3c). We can assume that the clear local distortions along the Q_x coordinate must originate from low-symmetry perturbations (strains) stemming from the distant ligand substituents which become vibronically enhanced in the way specified in refs 76–78 and 89.

To study this point, geometry optimizations on complexes **1**–**4** have been performed, where $Fe^{II}(d^6)$ has been replaced by $Mn^{II}(d^5)$, thus eliminating vibronic forces. Geometrical parameters r_i, α_{ij}, and β_{ij} along with values of ρ (defined in Figure 4) are listed in Table S1 (Supporting Information). For the stereochemically inactive Mn(II) the latter values reflect the net effect of the substituents on the geometry. As for Fe(II) the tiny distortions are dominated by displacements along the ε_d mode but are now of purely elastic origin. Values of $\rho(\varepsilon_d)$ for Mn(II) follow a clear trend increasing from complex **1** to **4** as shown in Figure 7, where for the sake of comparison the corresponding values of Fe(II) are presented. The results demonstrate in an impressive way the vibronic amplification of the distortions caused by the substituents R. The latter modify the bonding properties of the tpa^R ligand and therefore the vibronic coupling parameter F_ε. This will be the subject of the analysis in section III.4. In addition to the substituents, counterions and packing forces may also affect the geometry. Treatment and analysis of these effects is, however, beyond the scope of the present work and will require further theoretical development.

Apart from the effect of the substituents, our results clearly show that vibronic coupling in the complexes under study is weak. As emerges from consideration of a smaller model complex $[FeN_4H_9]^-$ (III) (Figure 6b) with axial NH_3 and three unlinked equatorial NH_2^- amido groups, we can attribute the rather weak Jahn–Teller activity to the rigid tpa ligand backbone; a geometry optimization starting from the FeN_4 coordination geometry, identical to (I), shows that the axial Fe–NH_3 bond is unstable. Upon geometry optimization the axial ligand tends to dissociate leading to $[FeN_3H_6]^-$ (complex IV, Figure 6c). A much larger Jahn–Teller activity in (IV) compared to (I) is obtained (Table 3c). However, in this system ^5E is an excited state as the d_{z2} orbital falls below the e set and hence $^5A_1$ becomes the lowest state. We conclude from these analyses that the tpa ligand plays a crucial role in regulating the electronic and steric

properties of the $[Fe(tpa^R)]^-$ series. The effect is 2-fold: first, the stiffness of the ligand suppresses at least to some extent the Jahn−Teller coupling of the ^5E ground state. Second, the axial Fe−N is imposed by the ligand, and thus, the ^5E ($e^3a_1{}^1e^2$) ground state is stabilized over the $^5A_1$ ($a_1{}^2e^2e^2$) state that otherwise would be the ground state.

The weak Jahn−Teller effect in the complexes under study leads to a situation in which SOC dominates over vibronic coupling (Figure 3); here the range of variation of δ is distinctly smaller than the value of ζ. The energy dependence of the two lowest states (A_1, A_2) and E on δ shows that the Jahn−Teller coupling in these states is completely quenched. This is just the opposite in the second excited state ($E(|M_J| = 1/2)$, Figure 3), which is not affected by SOC ($M_s = 0$ in this case). While the latter state is only weakly populated at the temperatures of the magnetic measurement, it may affect the structure at room temperature, thus supporting the distortions.[90]

III.2. Multiplet Structure and Effect of Spin−Orbit Coupling. The six d electrons of Fe(II) (Figure 5) give rise to 5 quintet states. Their SA-CASSCF and NEVPT2 energies obtained on the basis of the X-ray structures are listed in Table 4.

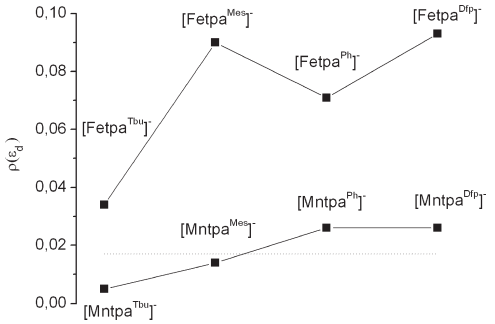

Figure 7. Extent of distortions as quantified by $\rho(\varepsilon_d)$ of $[Mn(tpa^R)]^-$ in comparison with those of their Fe(II) congeners from DFT geometry optimization; the value of $\rho(\varepsilon_d)$ resulting from the DFT geometry optimization of the truncated model complex $[MnN_4C_{15}H_{15}]^{1-}$ is shown by a horizontal dotted line.

The energies of all quintet states are computed to be lower than those of the triplet states (see section III.4 and Table 6a) with a sizable energy gap of 13 000 cm^{-1} between the ^5E ground state and the lowest triplet state. The rather small deviations from axial symmetry (vide supra) lead to a ground state splitting 2δ which increases progressively from 0 to 375 cm^{-1} across the series **1** < **2** < **3** < **4**. $Fe(tpa^{Tbu})$ complex **1**, which was reported to be strictly trigonal, possesses a 2δ of zero at the CASSCF level of theory which increases to $2\delta = 15$ cm^{-1} in NEVPT2. Clearly, this is an artifact of the contraction procedure used to define the first-order interacting space and is shared by all internally contracted electron correlation methods. Dynamical correlation effects accounted for at the NEVPT2 level of theory introduce energy shifts of the $^5E \rightarrow {}^5A_1$, $^5E \rightarrow {}^5E$ transitions by 2000−2500 cm^{-1} (to higher energy) and of the quintet to triplet transitions by 4000−5000 cm^{-1} (to lower energies) (Table 6a). The Jahn−Teller effect in the electronic ground state is rather weak because the degenerate orbital set involved only participates in π bonding. The excited ^5E state that has an uneven occupation in the degenerate, σ- and π-antibonding d_{xy} and d_{x2-y2} set of orbitals shows a much larger low-symmetry splitting (into $^5A'$ and $^5A''$, C_s symmetry) than the ground ^5E state (cf. Table 4).

Accounting for SOC leads to the energies of the sublevels included in Table 4. The energies of the lowest five sublevels follow on the trends obtained for δ, as depicted in Figure 3. As follows by a comparison of various sets of model calculations (Figure 8), the orthorhombic splitting of the first excited term E (Figure 3, ^5E, $E(|M_J| = 3/2)$) increases when extending the SOC matrix with the $^5A_1$ and ^5E excited states. It increases even more when the triplet excited states are also included. Moreover, the topmost level (Figure 3, ^5E, $E(|M_S| = 0)$) of the zero-field split $S = 2$ ground state drops down in energy when including excited quintet and triplet states in the CI treatment. It follows from Figure 8 that accounting for surrounding effects and extending

Table 4. Energies (in cm^{-1}) of $S = 2$ States and ^5E (C_3 parent symmetry notations) Components Split out by Spin−Orbit Coupling from CASSCF and NEVPT2 Calculations of the Four FeN_4 Complexes with Geometries from X-ray Diffraction Data and Accounting for the Complete Set of the 5 Quintet and 45 Triplet Electronic States[a]

	$[Fetpa^{Tbu}]^-$		$[Fetpa^{Mes}]^-$		$[Fetpa^{Ph}]^-$		$[Fetpa^{Dfp}]^-$	
electronic state[b]	CASSCF	NEVPT2	CASSCF	NEVPT2	CASSCF	NEVPT2	CASSCF	NEVPT2
^5E	0	0	0	0	0	0	0	0
	0.3	15.1	112.4	118.2	123.7	139.8	316.8	374.8
$^5A_1$	5011.4	7429.2	5103.4	7487.9	5102.7	7440.6	5386.2	7579.1
^5E	6701.8	8759.5	6426.4	8373.3	6773.7	8836.4	5972.1	7791.3
	6702.1	8760.1	7365.8	9611.5	7209.3	9432.1	6502.2	8511.1
A_1,A_2	0	0	0	0	0	0	0	0
	0.001	0.001	0.054	0.034	0.056	0.047	0.605	0.605
E	80.6	83.4	72.1	74.8	70.4	71.6	40.1	37.3
	80.6	83.5	76.2	78.2	74.8	75.8	52.2	49.0
E	170.7	168.2	124.4	126.8	120.1	119.3	67.2	61.8
	171.7	183.2	236.2	244.5	243.1	258.2	380.9	433.9
A_1	250.4	258.2	277.2	286.3	281.7	295.8	396.6	447.7
A_2	300.8	300.1	323.6	325.0	327.9	333.8	433.4	477.8
E	389.7	389.1	406.9	407.8	410.2	414.7	491.0	529.7
	389.8	389.2	407.8	408.6	411.2	415.6	493.4	531.7

[a] The state of lowest energy has been taken as energy reference. [b] Term notations are given for the D_3 holohedrized symmetry.

the set of active orbitals with ligand lone pairs does not alter the energy level structure. Finally, the effect of the remote substituents on the ground state spin sublevels emerges when comparing the results for the truncated model complex (I) with those including the entire ligand (exemplified in Figure 8 using complex **2**).

III.3. Magnetic Anisotropy. Compounds **1**−**4** have previously been magnetically characterized and were found, by both direct (dc) and alternating current (ac) susceptibility measurements, to be highly anisotropic.[1,2] Specifically, for **1** a large D of -48 cm^{-1} and a much smaller yet non-negligible $|E|_{max}$ = 0.4 cm^{-1} were deduced from a fit of the magnetization data employing a SH of eq 13. Aside from the approximations inherent in this particular choice of SH (see below), both (dc) and (ac) data show the presence of an orthorhombic anisotropy leading to an efficient tunneling pathway in all four complexes. Since these ions are non-Kramers systems, this implies low-symmetry splitting of the $\pm M_s$ pairs (described by the parameter E) and deviations from the apparent crystallographic symmetry in the 128 K X-ray structure. This is largely in agreement with the subtle distortions found by DFT for this and all other complexes investigated here (Table 2). Adopting the DFT structure and the ab initio results for this compound we plot in Figure 9 field-dependent magnetizations obtained directly from the ab initio calculations by using all SOC split sublevels of the ^5E ground state and their wave functions. There is reasonable agreement between computed and experimental data points with calculated values of the magnetization M being systematically higher than the experimental ones. A plot of the magnetization with a magnetic field oriented parallel (||) and perpendicular (⊥) to the pseudo C_3 axis nicely illustrates the almost Ising-type behavior of the anisotropy with a large and maximal $M_{||}$ and almost zero $M_{\perp}$ (Figure 9a). With a magnetic field oriented parallel to the x or y axis (see Figure 2 for their definitions) within the FeN_3 plane we further obtain $M_x > M_y$, implying a substantial transversal anisotropy and a negative value of the parameter E (see Figure 9b and eq S40, Supporting Information).

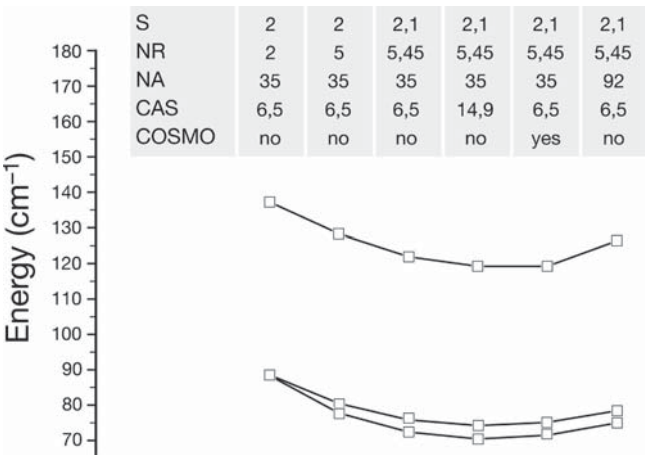

Figure 8. Effects of the spin states (S), number of roots (NR, i.e., number of nonrelativistic eingenvectors and eigenvalues used in construction of the SOC matrix) for each spin, adopted cluster model (NA, number of atoms), inclusion of solvent (COSMO), and space of active orbitals on the lowest three excited spin levels of $[Fe(tpa)^{Mes}]^-$ with the geometry from reported X-ray data.

The geometric and electronic structures of the investigated systems imply that a SH of the form of eq 14 is best suited for a comparison between theoretical and simulated data and to allow for an exploration of magneto-structural correlations. The parameters D, B_{40}, and $|E|$, obtained from a best fit to experimentally reported magnetizations and from the calculated lowest five SOC split sublevels, are presented in Table 5a. The sign of E could not be fixed from these considerations. However, based on calculations (e.g., Figure 9b) E is found to be negative in all complexes considered (see above). We note in passing that the values of these parameters are not equally well constrained by the two sets of data. While all three parameters D, B_{40}, and $|E|$ are apart from the sign of E (see above) accurately determined in the ab initio calculation they are subject to large error-bars when adjusted to fit the experimental magnetization data. In particular, for complexes **1** and **2**, which according to the ab initio results possess the largest $|D|$, no accurate fits could be achieved. For example, D is mainly determined from the third, fourth, and fifth levels, which are almost completely depopulated at the temperatures used in the experiments. D gets smaller when going to complexes **3** and **4**, and so the error bars of the experimentally fitted D, B_{40}, and E (σ = 0.013 (**4**) to be compared with σ = 0.024 (**1**), 0.029 (**2**), and 0.030 (**3**), see Table 5a). The more accurate best fit values of D, B_{40}, and E for complex **4** (see their error bars given in Table 5a) compare very well with the theoretically predicted ones (Table 5a). As illustrated in Figure 10, the low-field values

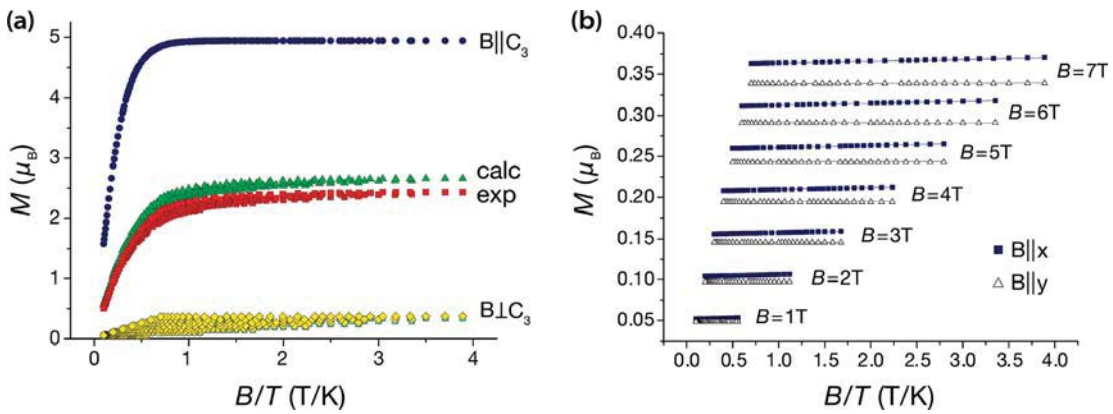

Figure 9. Theoretical (DFT-optimized geometry, NEVPT2) vs experimental field-dependent magnetizations for $[Fetpa^{Tbu}]^-$ (experimental data points are adopted from ref 2 and plotted using numerical data provided by the authors of this reference).

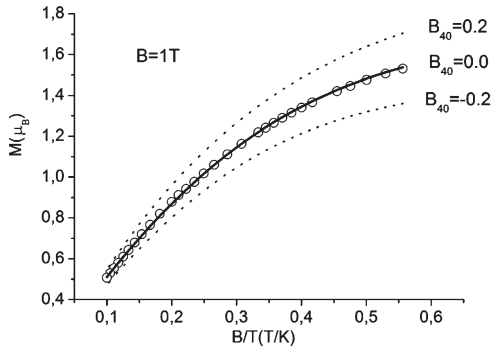

Figure 10. Experimental magnetization (M, B = 1 T, open circles) for complex **4** (adopted from ref 2 and plotted using numerical data provided by the authors of the cited work) and its values calculated using SH with $D = -10.30$ cm^{-1}, B_{40} = 0.0 cm^{-1}, E = 2.67 cm^{-1}, and g = 2.19 (solid line, see Supporting Information for details regarding the fit and Table 5a for standard deviations and parameter error bars). The variation of M with B_{40} (broken lines) is illustrated.

of M (B = 1 T) are found to be mostly affected by B_{40} (to be compared with Figure S4 showing much less variation of M (B = 1 T) with D, E, and g but see the changes of the high-field M (B = 7 T) with D, B_{40}, E, and g). Experimental[12] and simulated (using best-fit parameters from Table 5a) M data for complexes **1**−**4** are given in the Supporting Information (Figures S5−S9).

In spite of the uncertainty in determination of D, B_{40} for complexes **1** and **2** and to a lesser extent for complex **3** as well, there is good agreement between the ab initio and best fit to M data sets (Table 5a). In particular, the trend that $|D|$ decreases along the series is well reproduced. On the basis of these trends it was concluded in ref 2 that D rises with increasing ligand basicity tuned by the tpa substituents. A ligand field analysis (see section III.4) lends support to this proposal.

The comparison between the CASSCF and the NEVPT2 results shows that dynamical correlation effects do not play a leading role for the anisotropy; the values of D, B_{40}, and E obtained in the two treatments, the simple CASSCF and the more sophisticated NEVPT2, are quite similar (Table 5a). Good agreement between SA-CASSCF calculations and experiment was found in a number of previous studies.[13] By contrast, as pointed out above, the geometry that is adopted is of crucial importance. For example, for **2** D changes significantly from −29.1 cm^{-1}, obtained with the X-ray geometry, to −23.7 cm^{-1}, obtained with a DFT-optimized structure. Not unexpectedly, values of D resulting from calculations restricted to truncated model clusters (Table 5b) of the type of (I, see Figure 6a) do not display significant variations, which is in disagreement with both experiment and calculations on nontruncated models.

Importantly, it should be noted that there is an essential contribution of the fourth-order parameter B_{40} to U, the energy barrier for thermal relaxation of the magnetization (eq 29), which is found to be

$$U = -4D + 60B_{40} \tag{29}$$

This value is positive for complexes **1**−**4** and increases the value of U significantly by 24.6, 10.8, 9.0, and 2.0 cm^{-1}, respectively (NEVPT2, X-ray geometry). The values closely follow the trends in $|D|$. On the basis of on the comparison between the parameters D, B_{40} (Table 5a), and the values of the ^5E ground state

Table 5a. Theoretical and Experimental Values[a] of the Parameters of the Spin Hamiltonian D, B_{40}, and $|E|$ (in cm^{-1}) of tpa Complexes with Geometries from X-ray Diffraction Data and DFT Geometry Optimization[c]

	[Fetpa^{Tbu}]$^-$				[Fetpa^{Mes}]$^-$				[Fetpa^{Ph}]$^-$				[Fetpa^{Dfp}]$^-$			
	CASSCF	exp[b]	NEVPT2	CASSCF	exp[b]	NEVPT2	CASSCF	exp[b]	NEVPT2	CASSCF	exp[b]	NEVPT2	CASSCF	exp[b]	NEVPT2
D	−35.89	−47.5 (+7.5,−11.4)	−35.95 [−29.71]	−28.36	−37.5 (+5.0,−7.6)	−29.06 [−23.67]	−27.54	−27.5 (+1.6,−2.6)	−27.57 [−26.49]	−16.20	−10.3 (+0.27,−0.77)	−15.00 [−15.05]
B_{40}	0.45	0.30 (+0.37,−0.57)	0.41 [0.20]	0.18	0.30 (0.25,−0.39)	0.18 [0.09]	0.17	0.46 (+0.08,−0.13)	0.15 [0.14]	0.04	0.00 (+0.01,−0.03)	0.03 [0.03]
$\|E\|$	0.00	0.18 (+4.78)	0.00 [0.40]	0.69	0.18 (+4.27)	0.57 [0.99]	0.72	0.08 (+3.54)	0.69 [0.75]	2.01	2.67 (+0.30)	1.95 [1.91]

[a] Deduced from a fit to experimental field-dependent magnetization data[1−2] with error bars listed in parentheses (see Supporting Information for details regarding the fit and simulations). [b] Nonlisted g values and standard deviation (σ) between calculated and experimental magnetizations are [Fetpa^{Tbu}]$^-$ g = 2.28(±0.02), σ = 0.024; [Fetpa^{Mes}]$^-$ g = 2.20(+0.03,−0.02), σ = 0.029; [Fetpa^{Ph}]$^-$ g = 2.31(+0.025, −0.02), σ = 0.030; [Fetpa^{Dfp}]$^-$ g = 2.19(+0.01,−0.02), σ = 0.013. [c] NEVPT2 results pertaining to geometric structures from DFT geometry optimizations are given in square brackets.

Table 5b. Spin-Hamiltonian Parameters Obtained Using Truncated $[FeN_4C_{15}H_{15}]^{1-}$ Model Complexes with the Same Geometry As the Corresponding Nontruncated Complex

	$[Fetpa^{Tbu}]^-$		$[Fetpa^{Mes}]^-$		$[Fetpa^{Ph}]^-$		$[Fetpa^{Dfp}]^-$	
	exp. geometry	DFT geometry	exp. geom.	DFT geometry	exp. geometry	DFT geometry	exp. geometry	DFT geometry
D	−36.56	−31.96	−27.96	−31.53	−30.56	−30.08	−27.16	−30.34
B_{40}	0.46	0.28	0.17	0.27	0.23	0.23	0.16	0.24
$\lvert E\rvert$	0	0.17	0.57	0.26	−0.38	−0.35	0.64	0.32

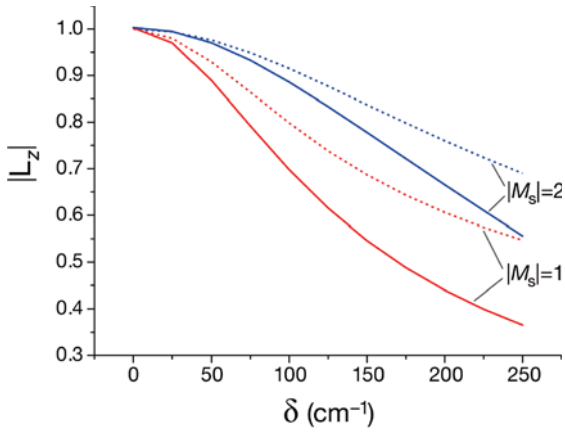

Figure 11. Expectation value of the orbital angular momentum operator within the ^5E state manifold as a function of the departure from C_3 symmetry (quantified by δ defined by one-half the ^5E splitting)): broken lines, in-state ^5E SOC only included; solid lines, SOC calculation with all 210 S = 2, 1, and 0 states taken into account. The plot has been constructed using the AOMX program package,[85] along with ligand field parameters obtained from a fit to CASSCF results for (**1**, Table 6b) allowing for a variation of δ.

splitting -2δ (Table 4) it follows that the magnetic anisotropy persists up to quite large values of δ. It stems from the unquenched ground state orbital momentum $|L_z|$ (Figure 10), which is reduced only slowly with increasing δ but depends on $|M_s|$ (Figure 11).[91] However, with increasing δ there is a drastic increase of the parameter E, which induces a tunneling splitting ΔE of the $M_s = \pm 1$ pair, 'shortcutting' the thermal relaxation barrier in this series to effective values that are far smaller than those predicted theoretically (eq 29). The interaction of the $M_s = \pm 2$ magnetic pair with the topmost $M_s = 0$ sublevel leads to a similar splitting given by perturbation theory according to eq 30.[92] It dominates the magnetic behavior at cryogenic temperature and explains the lack of blocking of the magnetization and hysteresis reported for all four systems.

$$\Delta E = \frac{3E^2}{-D + 15B_{40}} \tag{30}$$

Thus, both the second (E, D) and fourth-order term (B_{40}) can contribute to increasing ΔE and thus lead to a reduction of the anisotropy. Already small distortions δ lead to an increase of ΔE and thus to a low-temperature loss of magnetization dominated by quantum tunneling.

In a recent publication[93] it was claimed that "the splitting of the ^5E term cannot be described by a conventional zero-field splitting Hamiltonian proving the irrelevance of the spin-Hamiltonian formalism for FeN_4". As far as *all sublevels* of the ground state term ^5E are concerned this statement is certainly correct. However, because of the large sensitivity of the ^5E level splitting with respect to δ and because at the temperature of the experiments only the lowest five levels are thermally populated, we can still apply the SH of eq 14 in a slightly extended form compared to the usual form that involves only D and E (eq 13). Nevertheless, the SH of eq 14 is still fairly conventional.

Table 6. Energy Transitions (in cm^{-1}) of $[Fetpa^{Tbu}]^-$ from CASSCF and NEVPT2 calculations in Comparison with Their Values As Resulting from Ligand Field theory (a) Calculated Using Best-Fit Ligand Field Parameters (in cm^{-1}, b)[a]

(a) term	CASSCF	AILFT	NEVPT2	AILFT
$^5E(1) \rightarrow {}^5A_1$	5011	5011	7429	7429
$^5E(1) \rightarrow {}^5E(2)$	6702	6702	8760	8760
$^5E(1) \rightarrow {}^3A_2(1)$	17 698	17 626	12 929	13 083
$^5E(1) \rightarrow {}^3E(1)$	20 380	18 994	17 502	14 928
$^5E(1) \rightarrow {}^3E(2)$	21 390	21 649	18 509, 18 512	19 154
$^5E(1) \rightarrow {}^3E(3)$	21 805	21 903	19 296, 19 304	19 532
$^5E(1) \rightarrow {}^3A_2(2)$	22 693	22 780	20 305	20 348
$^5E(1) \rightarrow {}^3A_1(1)$	22 740	23 184	20 358	20 447
$^5E(1) \rightarrow {}^3E(4)$	23 896	24 487	20 763,20 764	22 258
$^5E(1)$				
$A_1A_2 \rightarrow E(1)$	80.6	75.4	83.4,83.5	80.1
$A_1A_2 \rightarrow E(2)$	171.0	163.9	168.2,183.2	171.2
$A_1A_2 \rightarrow A_1(2)$	250.4	236.5	258.2	247.0
$A_1A_2 \rightarrow A_2(2)$	300.8	309.9	300.1	308.2
$A_1A_2 \rightarrow E(3)$	389.8	391.5	389.1, 389.2	390.0

(b) parameter	CASSCF	NEVPT2	Fe^{2+}(free ion)
e_σ^e	5768	7540	
e_σ^a	1110	2330	
B	1785	1213	1058
C	3459	3372	3901
ζ	496	494	410

[a] Parameters for the free ion are taken from Griffith, J. S. *The Theory of Transition-Metal Ions*; University Press: Cambridge, 1971; p 437.

III.4. Ligand Field Analysis and Magneto-Structural Correlations. *III.4.1. Ligand Field Analysis of the ab Initio Results.* The X-ray structure of **1** is trigonal and, due to the degenerate irreducible representations in a perfect 3-fold symmetry, allows for an unambiguous assignment of the electronic transitions. Their values resulting from CASSCF and NEVPT2 calculations are listed in Table 6a. Neglecting first metal−ligand π overlap ($e_\pi = 0$, however, see below), ligand field matrix elements can been

Table 7. Angular Overall Model Parameters (in cm^{-1}) Deduced from a Fit of the Energies of the d−d Transitions (CASSCF results)[a]

	$[Fetpa^{Tbu}]^-$	$[Fetpa^{Mes}]^-$	$[Fetpa^{Ph}]^-$	$[Fetpa^{Dfp}]^-$
e^e_σ	5768	5374	4820	4246
e^a_σ	1110	1588	1941	2784
$e^e_{\pi s}$		570	1142	1119
ψ_1	11.9	8.6	1.7	6.8
ψ_2	11.9	10.9	1.6	3.2
ψ_3	11.9	3.8	2.2	3.3

[a] Data are based on the geometry as given by the X-ray structures.

expressed in terms of only two e_σ parameters describing the interaction between Fe(II) and the axial amino (e^a_σ) and the equatorial pyrrolyl (e^e_σ) ligands. The three-step procedure developed in section II.4 has been used to fit the ab initio data, resulting in computed (denoted by "AILFT" in Table 6a) energy levels and best-fit parameter values listed in Table 6b. Only five parameters afforded by LFT allow one to reproduce all the ab initio numerical data with remarkably consistency.[94]

On the basis of a comparison between the parameters B, C, and ζ for the free Fe(II) ion with the best-fit values to the CASSCF and NEVPT2, we conclude that the dynamical correlation introduced by NEVPT2 leads to a significant improvement for B and C compared to the values obtained from CASSCF. Even so, NEVPT2 values for B, C, and ζ are still larger than those reported for the free Fe^{2+} ion (Table 6b). This is a feature of the wave function contraction and the lack of electronic relaxation in second-order perturbation theory and hence cannot be cured with the present methodology. As elaborated in the Supporting Information using empirically corrected values of B and C (affording a reduction by 20%) does not affect D and B_{40}. However, both values get smaller by 30% when the same reduction of ζ is performed (relativistic nephelauxetic effect). CASSCF and NEVPT2 values of the parameters e^e_σ (5768 and 7540 cm^{-1}, Table 6b) are in good agreement with the ones deduced from highly resolved optical spectra of tetrahedral complexes of 3d metals, while e^a_σ appears to be too low.[95] The anomalously low value of e^a_σ is due to the stabilizing effect of s−d mixing which largely reduces the destabilizing antibonding effect due to the axial amine N ligand. It follows from a comparison of the CASSCF and NEVPT2 data that computed higher energy levels using the second approach are artificially split, a drawback that cannot be avoided while keeping to the perturbational approach.

Adopting the parameters B, C, and ζ obtained for complex (I) and continuing to use the CASSCF method for the aforementioned reasons, we list in Table 7 the best-fit values of e^e_σ and e^a_σ for the whole series. Here, due to the low-symmetry distortions small but positive values of $e^e_{\pi s}$ due to interactions between the Fe 3d orbitals and the out-of-plane π orbitals of tpa were deduced. Focusing further on e^e_σ, it is found that it increases along the series **4** < **3** < **2** < **1**. It is remarkable that this trend correctly reproduces the Lewis basicity and nicely fits with the increase of $|D|$ in the same direction (Figure 12), as postulated in a previous study.[2]

Following the same concept one should also expect that increasing π-donor basicity will act in the opposite direction. This is supported by the values of $e^e_{\pi s}$ that are found to increase from **2** to **3** and **4** (Table 7). This behavior will be analyzed in section III.4.2

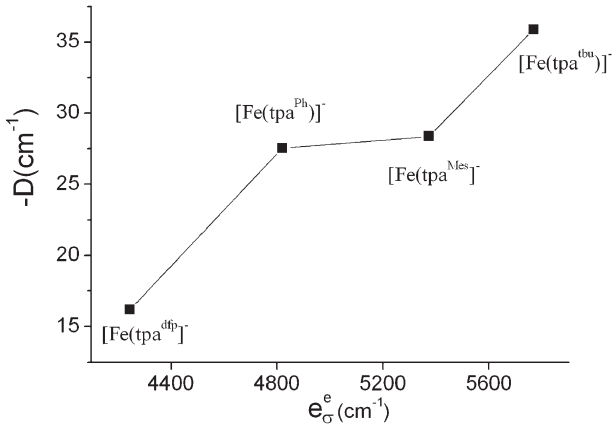

Figure 12. Correlation between the σ-donor ability of the tpa^R ligand (described by the parameter e^e_σ) and the axial zero-field splitting parameter D; data are based on the geometry as given by the X-ray structure.

The set of ligand field parameters deduced from the ab initio data provide a tool for the systematic search of new ligands which are better σ donors and thus expected to display enhanced magnetic anisotropies. To this end, we would like to stress the symbiosis between the theoretically rigorous ab initio approach and the approximate but intuitive and chemically more readily intelligible ligand field model.

III.4.2. Magneto-Structural Correlations. The parameters of the SH are complex and sensitive functions of small distortions of the geometry of $[Fe(tpa)]^-$ as discussed in sections II.2.2 and III.3 and of the chemical nature of the tpa^R ligands that is in turn fine tuned by the substituents R. The parametric structure of the AOM is ideally suited to separate these two effects and to study the effects of variations of the Lewis basicity of tpa^R induced by the substituents R as revealed by variations of the parameters e^e_σ and $e^e_{\pi s}$ in Table 7. For the sake of the analysis, we here adopt a FeN_4 geometry as given by the X-ray structure of $[Fe(tpa^{Mes})]^-$, the most distorted complex within the series. Taking the geometry as fixed we explore the dependence of the parameters δ, D, B_{40}, and E on e^e_σ and $e^e_{\pi s}$. Note that according to the sum rule, the trace of the ligand field matrix (here the sum over all ligands, $\Sigma = 3(e^e_\sigma + e^e_{\pi s}) + e^a_\sigma)$) is approximately invariant for complexes that have related coordination environments.[96] The ligand field analysis of d−d spectra for a variety of 3d ions in the +II oxidation state have shown that the trace $\Sigma^{exp} \approx 20\,000$ cm^{-1}.[97−101] This is pleasingly confirmed for the present systems as a value of $\Sigma^{AILF} \approx 19\,135 \pm 706$ cm^{-1} is obtained from the fitting of the AOM parameters to the ab initio data (Table 7). Upon inspection of Table 7 it is observed that not only Σ^{AILF} but also the sum $e^e_\sigma + e^e_{\pi s}$ pertaining to a given Fe−N(tpa) bond is (within ±300 cm^{-1}) constant (5760 cm^{-1}) along the series. Following this constraint, we plot in Figure 13a the dependence of δ on e^e_σ. It follows that an increase in the Lewis basicity (i.e., an increase e^e_σ) is accompanied by a reduction of δ.

This results (opposite to Figure 12 where purely electronic effects interfere with geometric distortion effects) in a smooth δ vs e^e_σ dependence. As expected, both D (Figure 13b) and B_{40} (Figure 13c) increase with e^e_σ. We can subdivide the net effect of the increasing Lewis basicity on the ground state magnetic

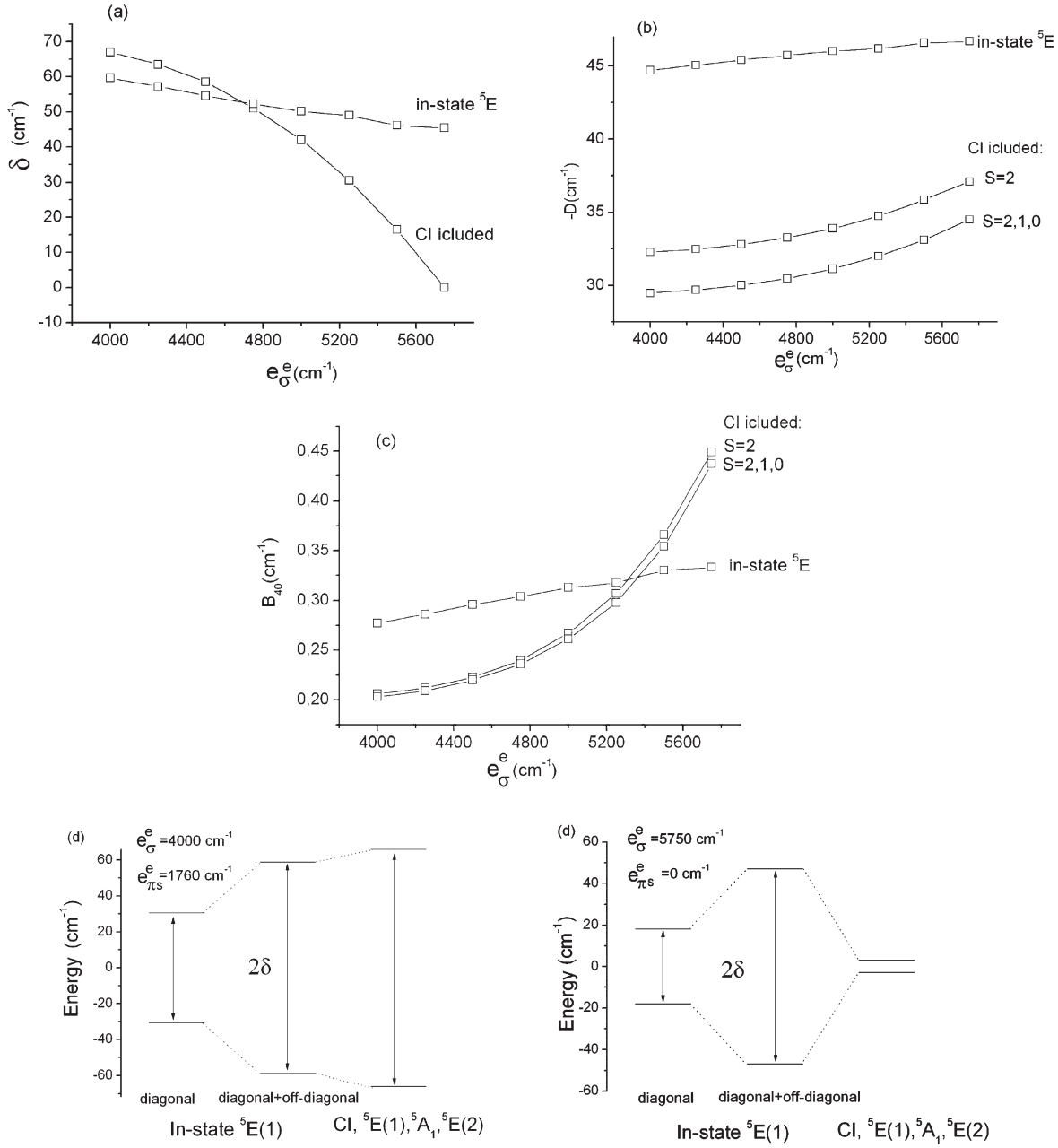

Figure 13. Dependence of δ (a), D (b), and B_{40} (c) on e^e_σ with and without configuration interaction between the ^5E ground term with ligand field excited states; (d) contributions to δ for two limiting cases of values for e^e_σ and $e^e_{\pi s}$: large $e^e_{\pi s}$ (left) and vanishing $e^e_{\pi s}$ (right).

anisotropy into electronic effects evolving within the ^5E electronic ground state (in-state SOC) and contributions from configurational mixing via SOC with excited state multiplets. Model calculations show (Figures 13a–c) that the bulk of the effect of the Lewis basicity originates from configuration interaction between the $^5E(1)$ ground state with the $^5A_1$ and $^5E(2)$ excited states. As follows from Figure 13a–c, inclusion of these excited states into the SOC matrix leads to drastic reduction in δ and this effect increases with e^e_σ. This is accompanied by a corresponding increase in D and B_{40}. By contrast, the extension of the SOC matrix with the $S = 1$ and 0 ligand field excited states induces smaller changes in these parameters. A small decrease in $-D$ and negligible change in B_{40} are calculated. Resolving δ into separate contributions from $e^e_{\pi s}$ and e^e_σ is possible by choosing the first set of values of e^e_σ and $e^e_{\pi s}$; e^e_σ = 4000 cm^{-1} and $e^e_{\pi s}$ = 1760 cm^{-1} (Figure 13d, left) and the last one - with e^e_σ =5750 cm^{-1} and vanishing $e^e_{\pi s}$(Figure 13d, right).

Focusing on the first set of parameters, a first-order splitting 2δ (Figure 13d, left, a diagonal effect described by the parameter δ_1 in eqs 9 and 10) of ^5E is observed. This is induced by weak $d_{xz,\,yz}$–ligand interaction of π type. Because the pyrrolide rings in these complexes are nearly (but not completely) perpendicular to the FeN_3 plane (cf. eq 27 and the values of ψ, Table 7) this effect is small. Allowing further for off-diagonal mixing between the $^5A'(xz)$ and $^5A''(yz)$ sublevels of the ^5E ground state (parametrized by the parameter δ_2 in eqs 9 and 10) leads to a further increase in 2δ (Figure 13d, left, middle), an effect dominated by e^e_σ. Finally, extending the SOC matrix with excited

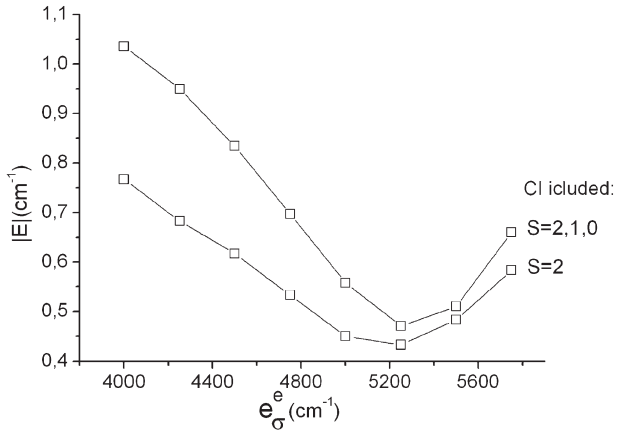

Figure 14. Dependence of the orthorhombic splitting parameter E on e^e_σ with and without configuration interaction with S = 1 and 0 states.

quintet states leads to an additional increase of 2δ, an effect related to deviations of the central Fe from the N_3 plane (θ = 82.2°, Table 2) and dominated again by e^e_σ. We conclude that with the parameter set (e^e_σ = 4000 cm^{-1}, $e^e_{\pi s}$ = 1760 cm^{-1}) both e^e_σ and $e^e_{\pi s}$ and SOC−CI mixing with excited states act in the same direction, namely, an increase of 2δ. A quite different situation exists if e^e_σ is large while $e^e_{\pi s}$ is vanishing (pure sigma-donor ligands; Figure 13d, right). Here, again, in-state ^5E electronic effects induce large splittings 2δ, which, however, become nearly zero when allowing for SOC−CI mixing with the excited states. This leads to an increase of D and B_{40}.

Recall (see section II.2.2) that an increase in 2δ is not always expected to affect the value of the orthorhombic zero-field splitting parameter E as far as ^5E in-state electronic effects are concerned. In fact, an accidental degeneracy of ^5E is obtained in this case (eqs 11). However, allowing for a SOC−CI mixing of the ^5E term of the ground state with excited states, an E vs e^e_σ curve with a minimum is calculated (Figure 14).

In contrast to D and B_{40}, extending the SOC model space from S = 2 to S = 2, 1, 0 leads to a significant increase of E. Nevertheless, with the distorted geometry of **2** we have not found a combination of ligand field parameters that would lead to the desirable situation of having an E value of zero, as would be required for SMM behavior. Thus, an exact 3-fold symmetry is mandatory to achieve this goal.

IV. CONCLUSIONS AND OUTLOOK

1 A general and transparent theoretical and computational scheme for interpretation and prediction of the magnetic properties of complexes with orbitally degenerate or nearly degenerate ground states was developed. The treatment is based on rigorous CASSCF/NEVPT2 calculations of the magnetic sublevels under the combined action of Jahn−Teller, low-symmetry, spin−orbit, and magnetic field perturbations. In this work we used this protocol to investigate the intriguing magnetic properties of a series of $[Fe(tpa^R)]^-$ complexes with a ^5E ground state.

2 A study of the multimode $^5E\otimes\varepsilon$ Jahn−Teller effect showed that vibronic coupling for these systems is largely suppressed by the rigid ligand backbone, with contributions from normal modes widely delocalized over the ligand macrocycle and concentrated in a narrow energy window below 250 cm^{-1}. The Jahn−Teller effect is further reduced by SOC. On the basis of this result, the observed distortions must be attributed to vibronic enhancement of low-symmetry perturbations due to the tpa substituents R and possibly also to crystal packing and counterion effects.

3 It was shown that the small geometric distortions reported in X-ray crystal structures of complexes **2**−**4**, which are possibly also present in the (yet unknown) low-temperature structure of complex **1**, are large enough to render application of a standard S = 2 spin Hamiltonian for description of their magnetic properties valid. However, a fourth-order anisotropy term, B_{40}, must be included in the analysis together with the standard second-order terms D and E. Values of these parameters adjusted to ab initio results and independently deduced from a reinterpretation of the reported magnetic data are consistent with each other and lend support to a concept correlating the value of D with the tpa^R ligand Lewis basicity.

4 A positive value of B_{40} emerging invariably from analysis of the ab initio results was found to yield a considerable contribution to the quantity U, the energy barrier for the thermal relaxation of the magnetization. From deduced values of E it is concluded that quantum tunneling is responsible for the systems relaxing much faster than expected from the theoretical value of the anisotropy barrier.

5 A ligand field interpretation of the ab initio data (AILFT) was used to deduce chemical bonding parameters within the framework of the angular overlap model. This approach allows for quantification and analysis of the correlation between the zero-field splitting parameter D and the σ-bond strength (represented here by the angular overlap parameter e^e_σ), which is finely tuned by the substituents on the tpa ligand. This is consistent with the proposal brought forward by the analysis of the experimental data.[2]

We hope that the theoretical and conceptual framework developed in this work as well as the detailed analysis of the Fe(II) complexes considered in the present study will further stimulate experimental efforts aimed at finding and characterizing mononuclear transition metal complexes with SMM behavior. We believe that prospects in this area are exciting.

■ ASSOCIATED CONTENT

Supporting Information. Details of formula derivations, procedures of fitting and simulations of magnetization data, computational details and geometries of complexes from X-ray data and optimized using DFT.

■ AUTHOR INFORMATION

Corresponding Author
*E-mail: mihail.atanasov@aci.uni-heidelberg.de (M.A.), neese@thch.uni-bonn.de (F.N.).

■ ACKNOWLEDGMENT

Financial support of this work by the Deutsche Forschungsgemeinschaft (SFB 813, "Chemistry at Spin Centers") is gratefully acknowledged. The authors thank Jeffrey R. Long and J. Zadrozny (University of Berkeley) for stimulating discussions and for critical reading of the manuscript prior to publication.

REFERENCES

(1) Freedman, D. E.; Harman, W. H.; Harris, T. D.; Long, G. J.; Chang, C. J.; Long, J. R. *J. Am. Chem. Soc.* **2010**, *132*, 1224.

(2) Harman, W. H.; Harris, T. D.; Freedman, D. E.; Fong, H.; Chang, A.; Rinehart, J. D.; Ozarowski, A.; Sougrati, M. T.; Grandjean, F.; Long, G. J.; Long, J. R.; Chang, C. J. *J. Am. Chem. Soc.* **2010**, *132*, 18115.

(3) Sessoli, R.; Gatteschi, D.; Caneschi, A.; Novak, M. A. *Nature* **1993**, *365*, 141.

(4) Mannini, M.; Pineider, F.; Sainctavit, P.; Danieli, C.; Otero, E.; Sciancalepore, C. A.; Talarico, M.; Arrio, M.-A.; Cornia, A.; Gatteschi, D.; Sessoli, R. *Nat. Mater.* **2009**, *8*, 194.

(5) Leuenberger, M. N.; Loss, D. *Nature* **2001**, *410*, 789.

(6) Ardavan, A.; Rival, O.; Morton, J. J. L.; Blundell, S. J.; Tyryshkin, A. M.; Timco, G. A.; Winpenny, R. E. P. *Phys. Rev. Lett.* **2007**, *98*, 057201.

(7) Stamp, P. C. E.; Gaita-Arino, A. *J. Mater. Chem.* **2009**, *19*, 1718.

(8) Torres, F.; Hernández, J. M.; Bohigas, X.; Tejada, J. *Appl. Phys. Lett.* **2000**, *77*, 3248.

(9) Gatteschi, D.; Sessoli, R.; Villain, J. *Molecular Nanomagnets*; Oxford University Press: New York, 2006 and references therein.

(10) Neese, F.; Solomon, E. I. *Inorg. Chem.* **1998**, *37*, 6568.

(11) Cirera, J.; Ruiz, E.; Alvarez, S.; Neese, F.; Kortus, J. *Chem.—Eur. J.* **2009**, *15*, 4078.

(12) Waldmann, O. *Inorg. Chem.* **2007**, *46*, 10035.

(13) Neese, F.; Pantazis, D. A. *Faraday Discuss.* **2011**, *148*, 229.

(14) Ako, A. M.; Hewitt, I. J.; Mereacre, V.; Clérac, R.; Wernsdorfer, W.; Anson, C. E.; Powell, A. K. *Angew. Chem., Int. Ed.* **2006**, *45*, 4926.

(15) Ishikawa, N.; Sugita, M.; Ishikawa, T.; Koshihara, S.-Y.; Kaizu, Y. *J. Am. Chem. Soc.* **2003**, *125*, 8694.

(16) Ishikawa, N.; Sugita, M.; Ishikawa, T.; Koshihara, S.; Kaizu, Y. *J. Phys. Chem. B* **2004**, *108*, 11265.

(17) AlDamen, M. A.; Clemente-Juan, J. M.; Coronado, E.; Martí-Gastaldo, C.; Gaita-Ariño, A. *J. Am. Chem. Soc.* **2008**, *130*, 8874.

(18) AlDamen, M. A.; Cardona-Serra, S.; Clemente-Juan, J. M.; Coronado, E.; Gaita-Ariño, A.; Martí-Gastaldo, C.; Luis, F.; Montero, O. *Inorg. Chem.* **2009**, *48*, 3467.

(19) Rinehart, J. D.; Long, J. R. *J. Am. Chem. Soc.* **2009**, *131*, 12558.

(20) Edelstein, N. M.; Lander, G. H. In *The Chemistry of the Actinide and Transactinide elements*, 3rd ed.; Morss, L. R., Edelstein, N. M., Fuger, J., Katz, J. J., Eds.; Springer: Dordrecht, 2006; Vol. IV.

(21) Orchard, A. F. *Magnetochemistry*; Oxford University Press: Oxford, 2003.

(22) Wybourne, B. G. *Spectroscopic Properties of Rare Earths*; Wiley: New York, 1965.

(23) Rinehart, J. D.; Harris, T. D.; Kozimor, S. A.; Bartlett, B. M.; Long, J. R. *Inorg. Chem.* **2009**, *48*, 3382.

(24) Benelli, C.; Gatteschi, D. *Chem. Rev.* **2002**, *102*, 2369.

(25) Laplaza, C. E.; Cummins, C. C. *Science* **1995**, *268*, 861.

(26) Yandulov, D. V.; Schrock, R. R. *Science* **2003**, *301*, 76.

(27) Atanasov, M.; Comba, P.; Daul, C. A. *Inorg. Chem.* **2008**, *47*, 2449.

(28) Atanasov, M.; Busche, C.; Comba, P.; Hallak, F. El; Martin, B.; Rajaraman, G.; van Slageren, J.; Wadepohl, H. *Inorg. Chem.* **2008**, *47*, 8112.

(29) Andres, H.; Bominaar, E. L.; Smith, J. M.; Eckert, N. A.; Holland, P. L.; Münck, E. *J. Am. Chem. Soc.* **2002**, *124*, 3012.

(30) Boča, R. *Coord. Chem. Rev.* **2004**, *248*, 757.

(31) Merrill, W. A.; Stich, T. A.; Brynda, M.; Yeagle, G. J.; Fettinger, J. C.; De Hont, R.; Reiff, W. M.; Schulz, C. E.; Britt, R. D.; Power, P. P. *J. Am. Chem. Soc.* **2009**, *131*, 12693.

(32) Reiff, W. M.; Schulz, C. E.; Whangbo, M.-H.; Seo, J. I.; Lee, Y. S.; Potratz, G. R.; Spicer, C. W.; Girolami, G. S. *J. Am. Chem. Soc.* **2008**, *131*, 404.

(33) Reiff, W. M.; LaPointe, A. M.; Witten, E. H. *J. Am. Chem. Soc.* **2004**, *126*, 10206.

(34) Popescu, C. V.; Mock, M. T.; Stoian, S. A.; Dougherty, W. G.; Yap, G. P. A.; Riordan, C. G. *Inorg. Chem.* **2009**, *48*, 8317.

(35) Harman, W. H.; Chang, C. J. *J. Am. Chem. Soc.* **2007**, *129*, 15128.

(36) Atanasov, M.; Daul, C. A.; Rauzy, C. *Struct. Bonding (Berlin)* **2004**, *106*, 97.

(37) Atanasov, M.; Daul, C. A.; Rauzy, C. *Chem. Phys. Lett.* **2003**, *367*, 737.

(38) Atanasov, M.; Comba, P. In *The Jahn-Teller Effect: Fundamentals and Implications for Physics and Chemistry*; Köppel, H., Barentzen, H., Yarkony, D. R., Eds.; Springer Series in Chemical Physics: Berlin, 2009; p 97.

(39) Malmqvist, P.-Å; Roos, B. O. *Chem. Phys. Lett.* **1989**, *155*, 189.

(40) Wolinski, K.; Pulay, P. *J. Chem. Phys.* **1989**, *90*, 3647.

(41) Andersson, K.; Malmqvist, P.-Å.; Roos, B. O.; Sadlej, A. J.; Wolinski, K. *J. Phys. Chem.* **1990**, *94*, 5483.

(42) Andersson, K.; Malmqvist, P.-Å.; Roos, B. O. *J. Chem. Phys.* **1992**, *96*, 1218.

(43) Roos, B. O.; Fülscher, M. P.; Malmqvist, P.-Å.; Serrano-Andrés, P. L.; Merchán, M. Theoretical Studies of the Electronic Spectra of Organic Molecules. In *Quantum Mechanical Electronic Structure Calculations with Chemical Accuracy*; Langhoff, S. R.; Ed.; Kluwer: Dordrecht, 1994.

(44) Roos, B. O.; Malmqvist, P.-Å. *Phys. Chem. Chem. Phys.* **2004**, *6*, 2919.

(45) Angeli, C.; Cimiraglia, R.; Malrieu, J.-P. *Chem. Phys. Lett.* **2001**, *350*, 297.

(46) Angeli, C.; Cimiraglia, R.; Evangelisti, S.; Leininger, T.; Malrieu, J.-P. *J. Chem. Phys.* **2001**, *114*, 10252.

(47) Angeli, C.; Cimiraglia, R.; Malrieu, J.-P. *J. Chem. Phys.* **2002**, *117*, 9138.

(48) Angeli, C.; Bories, B.; Cavallini, A.; Cimiraglia, R. *J. Chem. Phys.* **2006**, *124*, 054108.

(49) Maurice, R.; de Graaf, C.; Guihéry, N. *J. Chem. Phys.* **2010**, *133*, 084307.

(50) Maurice, R.; Bastardis, R.; de Graaf, C.; Suaud, N.; Mallah, T.; Guihéry, N. *J. Chem. Theory Comput.* **2009**, *5*, 2977.

(51) Maurice, R.; Guihéry, N.; de Graaf, C. *J. Chem. Theory Comput.* **2010**, *6*, 55.

(52) Maurice, R.; Pradipto, A. M.; Guihéry, N.; Broer, R.; de Graaf, C. *J. Chem. Theory Comput.* **2010**, *6*, 3092.

(53) Atanasov, M.; Comba, P. In *Structure and Function*; Comba, P., Ed.; Springer: Berlin, 2010; pp 74−79.

(54) Neese, F. *ORCA-an ab initio, Density Functional and Semiempirical program package* (v. 2.8-20); University of Bonn: Bonn, Germany, 2010.

(55) Perdew, J. P.; Burke, K.; Ernzerhof, M. *Phys. Rev. Lett.* **1996**, *77*, 3865. Perdew, J. P.; Burke, K.; Ernzerhof, M. *Phys. Rev. Lett.* **1997**, *78*, 1396.

(56) Grimme, S. *J. Comput. Chem.* **2006**, *27*, 1787.

(57) van Wüllen, C. *J. Chem. Phys.* **1998**, *109*, 392.

(58) Pantazis, D. A.; Chen, X. Y.; Landis, C. R.; Neese, F. *J. Chem. Theory Comput.* **2008**, *4*, 908.

(59) Weigend, F.; Ahlrichs, R. *Phys. Chem. Chem. Phys.* **2005**, *7*, 3297.

(60) Dyall, K. G. *J. Chem. Phys.* **1995**, *102*, 4909.

(61) Forsberg, N.; Malmqvist, P.-Å. *Chem. Phys. Lett.* **1997**, *274*, 196.

(62) Camacho, C.; Cimiraglia, R.; Witek, H. A. *Phys. Chem. Chem. Phys.* **2010**, *12*, 5058.

(63) Ganyushin, D.; Neese, F. *J. Chem. Phys.* **2006**, *125*, 024103.

(64) McWeeny, R. *Methods of Molecular Quantum Mechanics*; Academic Press: London, 1992.

(65) Neese, F. *J. Chem. Phys.* **2005**, *122*, 34107.

(66) Ganyushin, D.; Neese, F. *J. Chem. Phys.* **2006**, *125*, 024103.

(67) Klamt, A.; Schüürman, G. *J. Chem. Soc., Perkin Trans.* **1993**, *2*, 799.

(68) Klamt, A. *J. Phys. Chem.* **1996**, *100*, 3349.

(69) $|^5E,1\rangle$ and $|^5E,-1\rangle$ can mix with $|^5A_1,0\rangle$ via L_x and L_y which can become a pathway for quenching $|L_z|$ as is the case in T_2 states (cubic symmetry) where all three terms become degenerate. To a lesser extent this mechanism becomes operative in weakly distorted octahedral complexes, where due to weak π bonding the $|^5E, \pm 1\rangle - |^5A_1,0\rangle$

energy separation is small, easily tunable, and the mixing effective (see refs 70−74).

(70) Fishman, R. S.; Reboredo, F. A. *Phys. Rev. Lett.* **2007**, *99*, 217203.

(71) Fishman, R. S.; Okamoto, S.; Reboredo, F. A. *Phys. Rev. Lett.* **2008**, *101*, 116402.

(72) Fishman, R. S.; Reboredo, F. A. *Phys. Rev. B* **2008**, *77*, 144421.

(73) Reis, P.; Fishman, R. S.; Reboredo, F. A.; Moreno, J. *Phys. Rev. B* **2008**, *77*, 174433.

(74) Fishman, R. S.; Okamoto, S.; Reboredo, F. A. *Polyhedron* **2009**, *28*, 1740.

(75) Neese, F.; Solomon, E. I. *Magnetoscience-From Molecules to Materials*; Miller, J. S., Drillon, M., Eds.; Wiley-VCH: Weinheim, Germany, 2003; Vol. IV.

(76) Bersuker, I. B. *The Jahn-Teller Effect and Vibronic Interactions in Modern Chemistry*; Plenum Press: New York and London, 1984.

(77) Bersuker, I. B. *The Jahn-Teller Effect*; Cambridge, University Press: Cambridge, U.K., 2006.

(78) Bersuker, I. B.; Polinger, V. Z. *Vibronic Interactions in Molecules and Crystals*; Springer: Berlin, 1989.

(79) van Vleck, J. H. *Phys. Rev.* **1940**, *57*, 426.

(80) Schäffer, C. E.; Jørgensen, C. K. *Mol. Phys.* **1965**, *9*, 401.

(81) Schönherr, T. *Top. Curr. Chem.* **1997**, *191*, 88.

(82) Larson, E.; LaMar, G. N. *J. Chem. Educ.* **1974**, *51*, 633.

(83) Bridgeman, A. J.; Gerloch, M. *Prog. Inorg. Chem.* **1996**, *45*, 179.

(84) Figgis, B. N.; Hitchman, M. A. *Ligand Field Theory and Its Applications*; Wiley-VCH: NewYork, 2000.

(85) Adamsky, H. with contributions from Hoggard, P. E; Atanasov, M.; Eifert, K. *AOMX*, http://www.aomx.de.

(86) Ceulemans, A.; Beyens, D.; Vanquickenborne, L. G. *J. Am. Chem. Soc.* **1984**, *106*, 5824.

(87) Ceulemans, A.; Vanquickenborne, L. G. *Struct. Bonding (Berlin)* **1989**, *71*, 125.

(88) In the present case the results are identical with those following a procedure developed in McNaughton, R. L.; Roemelt, M.; Chin, J. M.; Schrock, R. R.; Neese, F.; Hoffman, B. M. *J. Am. Chem. Soc.* **2010**, *132*, 8645 because the vibronic coupling is weak. In this procedure an explicit potential surface scan is performed where one is moving along the eigenvectors of the Hessian obtained from a geometry optimization and subsequent frequency calculation using a CAS(6,5) wavefunction for the lowest two quintet roots of (I) (a 1:1 averaging over the two components of ^5E is performed, thus eliminating complications in the force field due to interfering quadratic vibronic coupling terms).

(89) The concept of vibronic enhancement is intimately related to the form of the lower sheet of the adiabatic potential energy surface of the linear $E\otimes\varepsilon$ problem. It consists of formation of an additional well on the circular trough with the Jahn−Teller radius ρ_o at a point given by φ_o. While external forces determine the value of φ_o at low cost of energy (W), the intrinsic Jahn−Teller forces determine the value of ρ_o and the energy stabilization E_{JT} ($E_{JT} \gg W$); the small distorting perturbation becomes vibronically amplified in magnitude given by the factor E_{JT}/W.

(90) The complete quenching of the vibronic forces by SOC in systems with orbitally degenerate ground states is by no means a general phenomenon. Thus, in cyanide-bridged Cu−Fe and Ni−Fe dimers with a rather strong Fe−CN bond and therefore more pronounced $T_2\otimes\varepsilon$ type Jahn−Teller coupling ($^2T_2$ low-spin ground state of Fe(III)) an opposite situation has been found by theory (cf. Figure 8, ref 27) and experiment (ref 28).

(91) Similar effects of $|L_z|$ on the magnetic anisotropy has been discovered (see refs 70−74 and references cited therein) in Fe(II)Fe(III) bimetallic oxalates. Here, because of the closer proximity of the $^5A_1$ excited to the ^5E ground state (both are stemming from the $^5T_2$ (O_h) parent term subject to weaker π-antibonding effects) $|L_z|$ quenching is larger and increases with temperature. This leads to interesting phenomena, such as magnetic compensation (reversal of the sign of the magnetization with temperature) and an inverse Jahn−Teller effect (low-temperature quenching of Jahn−Teller distortions due to increase of $|L_z|$).

(92) Using the values of D, B_{40}, and E and eq 30 the ab initio values of ΔE (in cm^{-1}, experimental geometry, CASSCF) are perfectly reproduced: calculated using D, B_{40}, E (ab initio data Table 4): complex **2**, 0.046(0.054); complex **3**, 0.052(0.056); complex **4**, 0.72(0.605).

(93) Palii, A. V.; Clemente-Juan, J. M.; Coronado, E.; Klokishner, S. I.; Ostrowsky, S. M.; Reu, O. S. *Inorg. Chem.* **2010**, *49*, 8073.

(94) Owing to the proximity of charge transfer states at higher energies, a procedure involving fitting all ab-initio-calculated transitions does not appear to be practicable.

(95) Lever, A. B. P. *Inorganic Electronic Spectroscopy*, 2nd ed.; Elsevier: Amsterdam, 1984.

(96) Deeth, R. J.; Gerloch, M. *Inorg. Chem.* **1985**, *24*, 1754.

(97) A justification of this empirical sum rule based on the effective Hamiltonian theory within the framework of first-principles quantum chemistry has been given in refs 98−101. The Σ value reflects the overall ligand-to-metal electron charge donation and its near-constancy may be regarded as an energetic equivalent of the electroneutrality principle.

(98) Woolley, R. G. *Chem. Phys. Lett.* **1985**, *118*, 207.

(99) Woolley, R. G. *Mol. Phys.* **1981**, *42*, 703.

(100) Gerloch, M.; Harding, J. H.; Woolley, G. G. *Struct. Bonding (Berlin)* **1981**, *46*, 1.

(101) Bridgeman, A. J.; Gerloch, M. *Prog. Inorg. Chem.* **1997**, *45*, 179−281, p 238, Table III.